Commensal virome regulate intestinal nutrient sensing via Th17 cells

Abstract

Our study explores the influence of gut virome on nutrient sensing via T cells in the small intestine. We discovered that the gut virome can independently affect the digestion and absorption of carbohydrates in the small intestine, and this effect is contingent upon T cell surveillance. Additionally, our research reveals heterogeneous responses elicited by virome components across different small intestinal cell types. Stimulation of intestinal epithelial cells is dependent on intact viral particles, while the stimulation of T cells and antigen-presenting cells relies on viral capsids. In the normal murine gut, the virome stimulates antigen-presenting cells to recruit T cells and induce IL22 expression. These findings are significant for developing therapeutic and nutritional strategies targeting metabolic diseases, underscoring the importance of incorporating the gut virome as a key element in interventions.

Introduction

The gut, a central organ for nutrient digestion, absorption, and immunity, is home to a diverse array of microorganisms. While the bacterial component of the gut microbiome has been the subject of extensive research, recent studies have shifted focus towards the gut virome, particularly bacteriophages, and their role in maintaining gut homeostasis[1].

The gut virome is known to influence disease states such as obesity and chronic social stress, primarily through interactions with gut bacteria[2,3]. However, emerging evidence suggests that the virome also directly engages with eukaryotic cells, potentially exerting a significant impact on their function[4]. Given the widespread application of bacteriophages

in industries such as food processing, vaccine production, and drug delivery[5,6], understanding the functional interactions between the human host and gut virome is of paramount importance.

Existing research suggests that immune cells can regulate how intestinal epithelial cells perceive nutrients, yet the underlying mechanisms are still not fully understood[7,8]. In this study, we strive to shed light on the role of the gut virome in modulating the gastrointestinal sensing of nutrients. Our findings suggest that the gut virome can independently influence the digestion and absorption of carbohydrates, with the effects varying based on the surveillance of T cells. These observations emphasize the gut virome's dual role in metabolic-immune modulation and highlight the complex interactions among various microbial communities within the gut ecosystem.

Result

Commensal gut viruses affect gut carbohydrate digestion and absorption

To explore the potential role of the gut virome in macronutrient metabolism, we utilized a mouse model to examine the impact of the gut virome on energy metabolism in response to different diet (Figure 1B and table S1). Mice were subjected to either a normal chow diet or a high-fat diet (HFD) consisting of 60% fat, with the addition of an antiviral cocktail (AVC) in drinking water (Figure 1A). We aimed to assess gut virome’s impact on macroscopic growth parameters (MGP) such as body weight, body length, and feed conversion ratio (FCR).

As expected, a 60% HFD resulted in increased body weight and decreased FCR compared to the chow diet, with no impact on body length[9] (Figure 1C, 1D, and S1A).

Histological examination revealed enhanced lipid accumulation in the liver and epididymal white adipose tissue (E-WAT) in the HFD group (Figure 1F and 1G). Interestingly, within the same dietary context, AVC administration in chow-fed mice led to increased body weight and decreased FCR, but no significant alterations were observed in HFD-fed mice (Figure 1C and 1D).

Given the selective impact of AVC on chow-fed mice, we hypothesized that its influence on MGPs might be carbohydrate-dependent. The introduction of a 45% HFD produced similar AVC effects as observed with the chow diet (Figure 1C and 1E). The absence of changes in food intake, body length, and lipid accumulation in the liver and E-WAT suggests that the AVC-induced modifications in MGPs were not due to effects on hypothalamic feeding centers, drug side effects, or changes in fat tissue energy storage (Figure 1F, 1G, S1A, and S1B). Taking into account the nutrient-absorbing capacity of the gut microbiota[10], we conducted bacterial plating assays and found no significant changes in fecal bacterial counts but a notable reduction in virus-like particles (VLPs) following AVC treatment (Figure S1C and S1D). These findings imply that the observed AVC effects might be associated with the regulation of carbohydrate digestion and absorption (CD&A) within the gut.

Given the potential dependency of the AVC effect on the regulation of CD&A in the small intestine, we subsequently measured fasting blood glucose levels and conducted oral glucose tolerance tests (OGTT) in chow-fed mice. We discovered that AVC treatment led to increased fasting blood glucose and impaired glucose tolerance (Figure 1H and I). These results suggest that the gut virome may have the ability to regulate the speed and efficiency of CD&A in the small intestine.

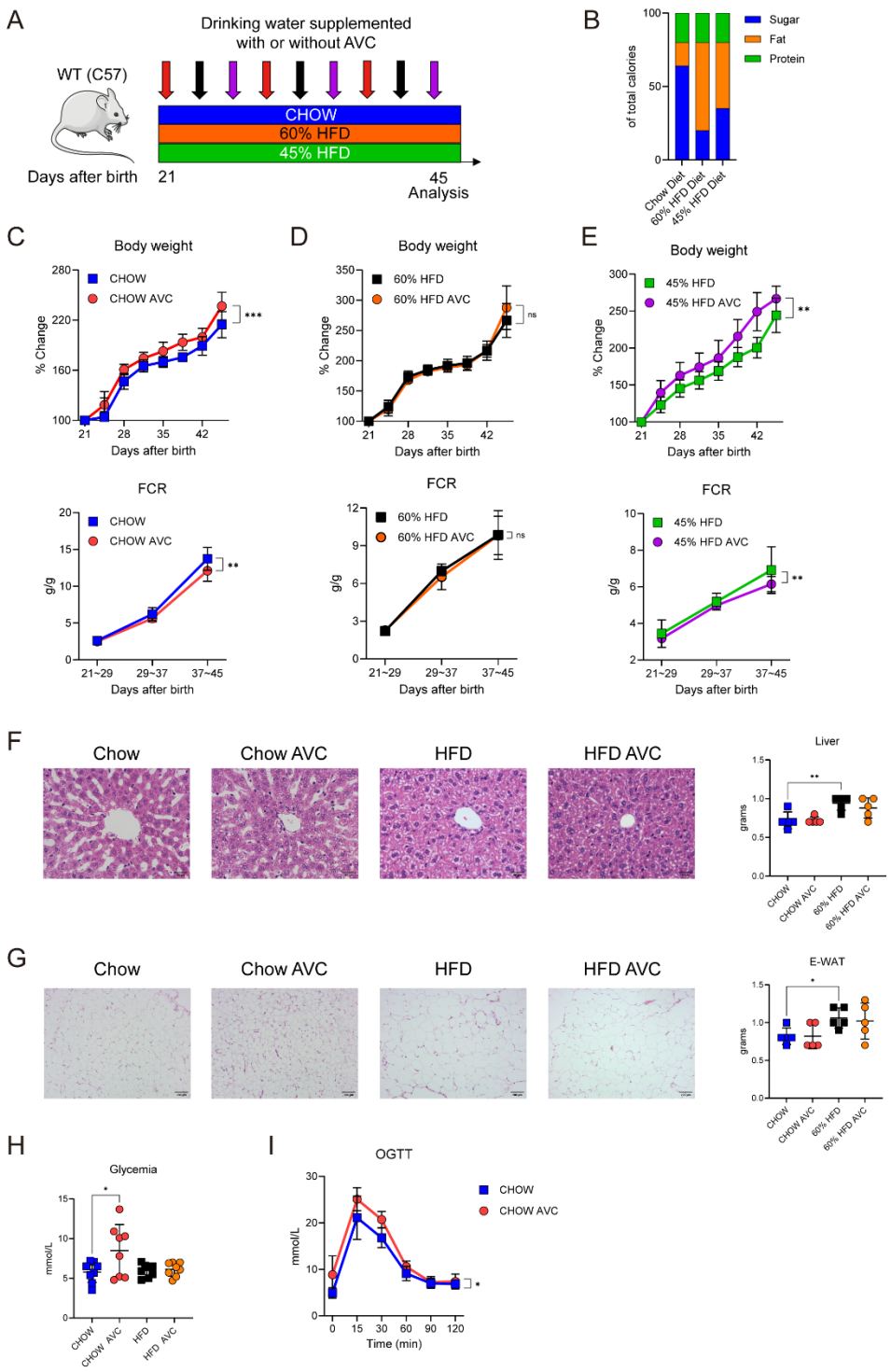

Figure 1. Commensal gut viruses affect gut carbohydrate digestion and absorption.

(A) Experimental scheme for (C-E).

(B) Schematic of the components of each diet, expressed as a percentage of total calories.

(C-E) Body weight and FCR in mice on a (C) chow diet, (D) 60% HFD and (E) 45%HFD. n = 6-8 mice/group.

(F-G) Liver and E-WAT weight variation in mice fed chow diet and HFD with or without AVC, followed by HE staining of paraffin sections. n = 5.

(H-I) Fasting blood glucose levels (H) and OGTT test (I) compared between different diet and AVC traetment. n = 5-8.

(C), (D), (E) and (I) represent mean ± SD analyzed by two-way ANOVA with Geisser-Greenhouse correction. (F), (G) and (H) represents mean ± SD analyzed by Student's t-test. Data combined from two independent experiments. $*p < 0.05$, $**p < 0.01$, $***p < 0.001$.

See also Figure S1

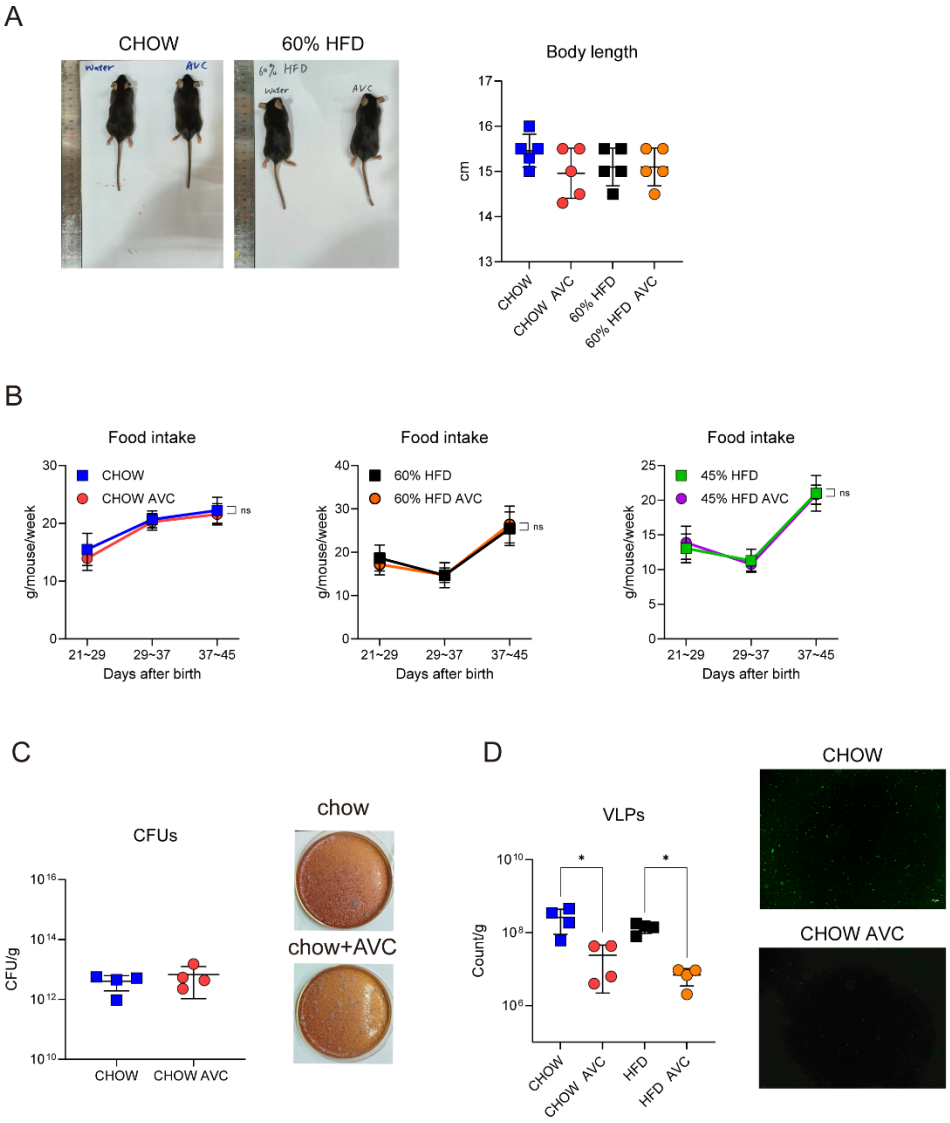

Figure S1. Commensal gut viruses affect gut carbohydrate digestion and absorption. Related to Figure 1

(A) Body length comparison in mice fed chow diet and 60% HFD with or without AVC. n = 5 mice/group.

(B) Food intake in mice on a chow diet, 60% HFD and 45% HFD. n = 6-8 mice/group.

(C) Representative images of bacteria culture analysis on CBA plates for chow and chow AVC treatment mouse cecal content.

(D) Confocal imaging and the count of SYBR Gold-stained VLPs isolated from the cecum of mice of chow and chow AVC group.

(A) represent mean ± SD analyzed by two-way ANOVA with Geisser-Greenhouse

correction. (B), (C) and (D) represents mean ± SD analyzed by Student's t-test. Data combined from two independent experiments. ∗$p < 0.05$.

Bacteriome cannot explain MGP and blood glucose caused by antiviral cocktail

Investigating the gut bacteriome's influence on AVC-induced metabolic changes, we analyzed cecal bacteriome profiles in chow-fed mice. AVC treatment preserved α-diversity but shifted β-diversity, suggesting a restructured bacteriome (Figure. 2A-2C, S2A).

Comparative analysis with the Disbiome database[11], which links bacteria to metabolic disorders, identified 17 bacterial genera associated with glucose metabolism disorders and obesity from 409 studies (Table S2). Among these, *Akkermansia*, known for its beneficial metabolic effects[12], was reduced in the AVC group, suggesting a potential link to the treatment's obesogenic impact (Figure 1D). Conversely, *Escherichia*, often abundant in glucose metabolic disorder population, unexpectedly decreased following AVC treatment (Figure. 1D).

LEfSe analysis identified distinct bacterial genera between the AVC-treated and control groups, highlighting the specific microbial shifts associated with AVC treatment (Figure. S3A). However, MicrobiomeAnalyst's Taxon Set Enrichment Analysis (TSEA) did not link AVC-specific bacteria to established metabolic disorder disease bacteriome profiles[13] (Figure. S3C, Tables S3).

Correlation analysis indicated a negative association between *Akkermansia* abundance and FCR, but no significant correlation was observed with the OGTT (Figure. 2I).

Interestingly, *Granulicatella* and *Psychrobacter*, less studied in metabolic disease, showed positive correlations with OGTT and negative with FCR (Figure. 2I). These bacteria potentially associated with the pathogens of culture-negative infective endocarditis[14,15]. Additionally, *Intestinimonas*, a butyrate producer[16], correlated positively with FCR and negatively with OGTT (Figure. 2I), supporting butyrate's reported benefits on glucose homeostasis and fat metabolism[17].

To determine the influence of specific bacterial taxa on AVC-induced phenotypes, we administered a low-dose of ampicillin (AMP) to mice. This intervention significantly modified microbial diversity without altering total bacterial counts (Figure 2A, 2B, 2E, 2F and S2B and S2D). After AMP treatment, *Intestinimonas*, *Granulicatella*, and *Psychrobacter* were almost undetectable (Figure 2G and S2E). RDA analysis revealed distinct effects of AMP and AVC on the bacteriome (Figure S2E). Additionally, AVC consistently induced changes in *Akkermansia*, *Odoribacter*, *Bacillus*, and *Vibrio* in both the AMP and CON backgrounds (Figure S2C).

Investigating the metabolic impact, AMP treatment alone did not affect body weight but increased the FCR and impaired glucose tolerance (Figure. 2H). These results underscore the gut bacteriome's significant role in metabolic processes. Remarkably, AVC treatment in the AMP context mirrored the metabolic effects seen in the CON group, suggesting a robust AVC-induced phenotype independent of the altered bacteriome (Figure. 2H). Correlation analysis implicated *Ruminococcus*, *Clostridia*, and *Hungatella* in AVC-induced changes in AMP background, yet these correlations did not hold in the CON background (Figure. 2J and S2G). Discrepancies emerged when comparing bacterial strains post-AMP AVC treatment with Disbiome database predictions. For instance, *Lachnospira*, typically enriched in glucose metabolic disorder patients, increased, while *Lactobacillus*, associated with healthy controls, also showed an increase (Figure. 2D). TSEA linked both AMP and AMP AVC signature LEfSe genera to microbiota signatures associated with diabetes and obesity (Figure. S3B, S4D, Tables S4).

Furthermore, PICRUST KEGG function prediction analysis indicated that AVC treatment does not affect carbohydrate metabolism or glycan synthesis and metabolism pathways in either CON or AMP backgrounds (Figure S3E).

In summary, we concur that the bacteriome also plays a crucial role in regulating intestinal CD&A. However, we have not identified a specific bacterium that can explain why AVC elicits similar effects in both CON and AMP backgrounds.

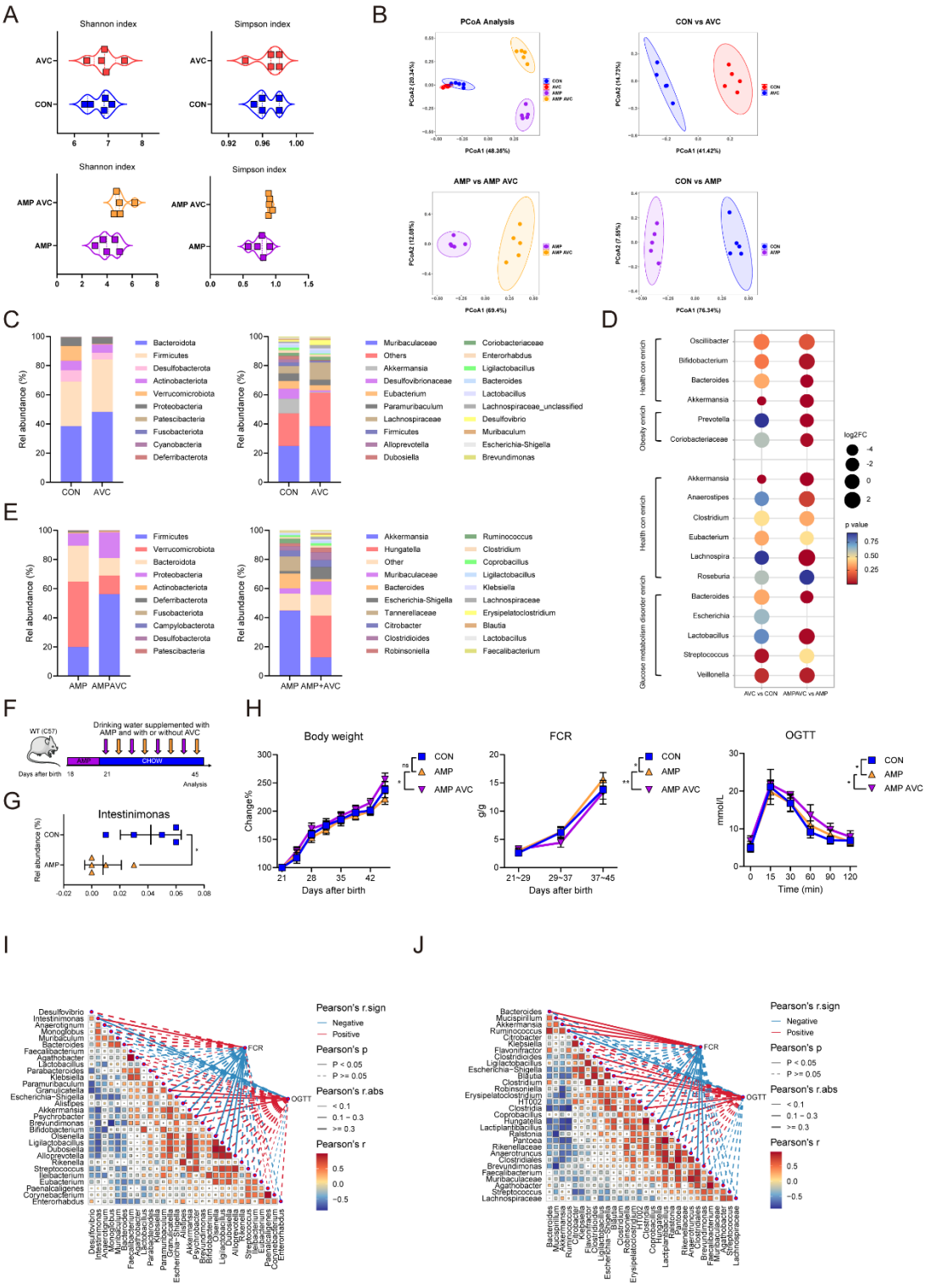

Figure 2. Bacteriome cannot explain MGP and blood glucose caused by antiviral cocktail. (A) Shannon's and Simpson's diversity for the cecal bacteriomes. Kruskal-Wallis test, followed by Wilcoxon's rank sum test with Bonferroni's correction, was conducted for alpha diversity. n = 5 mice/group.

(B) Principal co-ordinates analysis (PCoA) of 16S rRNA sequencing of cecal content at the operational taxonomic unit level. n = 5 mice/group.

(C) and (E) Community barplot analysis of 16S rRNA sequencing of cecal content from (C) CON background and (E) AMP background at the genus level. n = 5 mice per group.

(D) Bubble chart is used to display the bacteria related to glucose metabolism disorders and obesity in the Disbiome database. Inclusion criteria: sample: feces, control: healthy control, disease elevated genus-control elevated genus≥3 or disease reduced genus-control reduced genus≥3. The color of the bubbles represents the p-value, and the size of the bubbles represents log2FC.

(F) Experimental scheme for (H).

(G) Related abundance of *Intestinimonas* in the cecal content of AMP background mice. n = 5 mice/group.

(I-J) The relationship between bacteria genus and FCR and OGTT in (I) CON and (J) AMP background was calculated. The significant levels of Pearson's correlation among dependent variables were indicated by square size. Network planning showed the Pearson’s correlation between top 30 bacteria genus and FCR and OGTT. Red lines indicate positive correlations, while blue lines indicate inverse correlations. Edge width corresponds to Pearson’s r value, and edge type indicates statistical significance. Pearson's correlation coefficient matrix shows the relationships among dependent bacteria genus. The significant levels of Pearson's correlation among dependent bacteria genus were indicated by square size. Normality and Lognormality of FCR and OGTT were tested by Kolmogorov-Smirnov test, $p>0.1$.

(G) represents mean ± SD analyzed by Mann-Whitney test. Data combined from two independent experiments. (H) represent mean ± SD analyzed by two-way ANOVA with Geisser-Greenhouse correction. Data combined from two independent experiments. $*p < 0.05$, $**p < 0.01$.

See also Figure S2 and S3

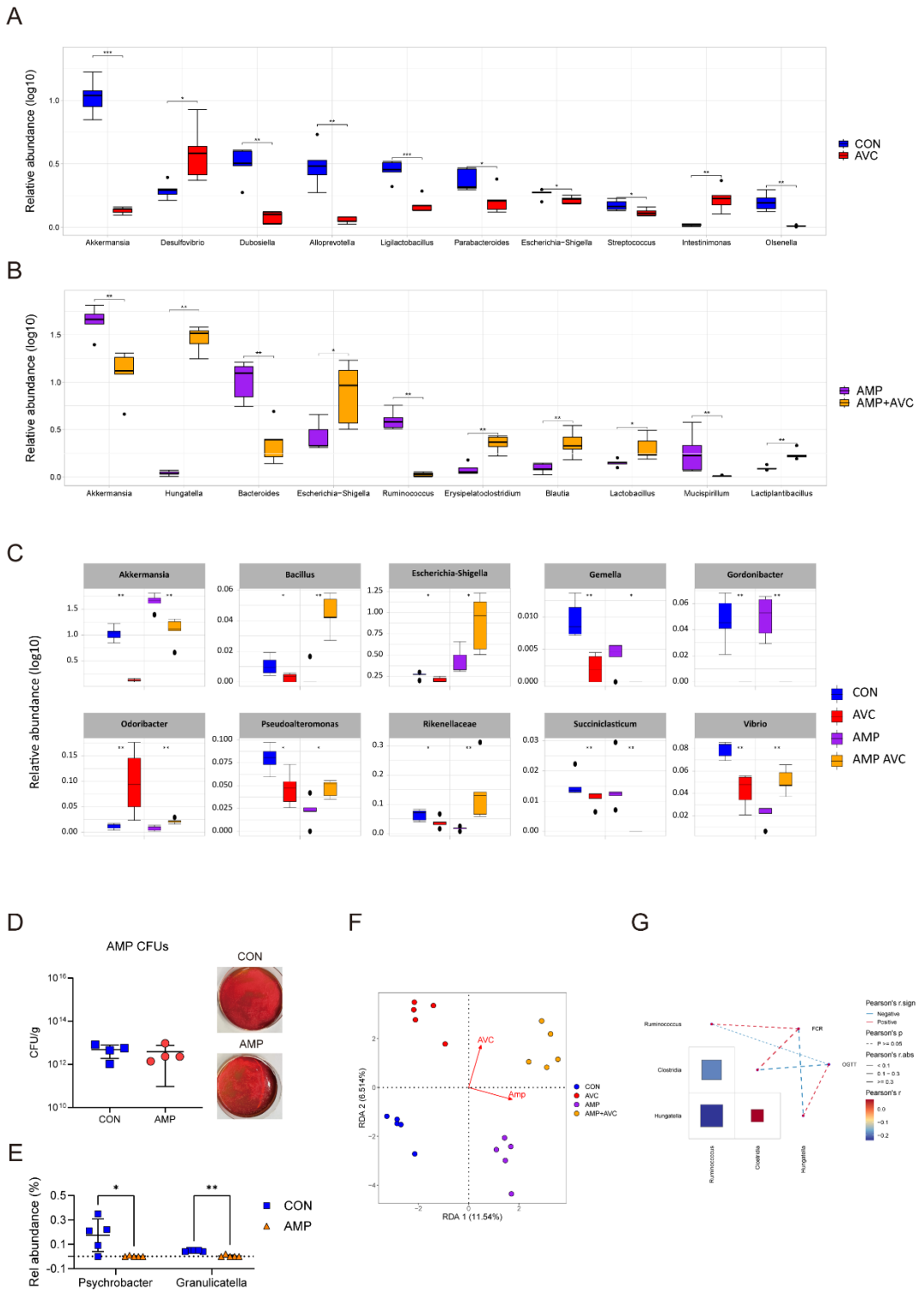

Figure S2. Bacteriome cannot explain MGP and blood glucose caused by antiviral cocktail. Related to Figure 2

(A-B) Relative abundance of top 10 bacteria genus in the cecal bacteriome in (A) CON and (B) AMP background. n = 5 mice/group

(C) Relative abundance of bacteria genus changed by AVC treatment both in CON or AMP background. n = 5 mice/group

(D) Representative images of bacteria culture analysis on CBA plates for CON and AMP treatment mouse cecal content. n = 4 mice/group

(E) Related abundance of *Psychrobacter* and *Granulicatella* in the cecal content of AMP background mice. n = 5 mice/group.

(F) RDA and CCA analysis of bacteriome and the treatment of AVC and AMP.

(G) Pearson's correlation of candidate bacteria and FCR and OGTT.

(A-D) represents mean ± SD analyzed by Mann-Whitney test. *p < 0.05, **p < 0.01.

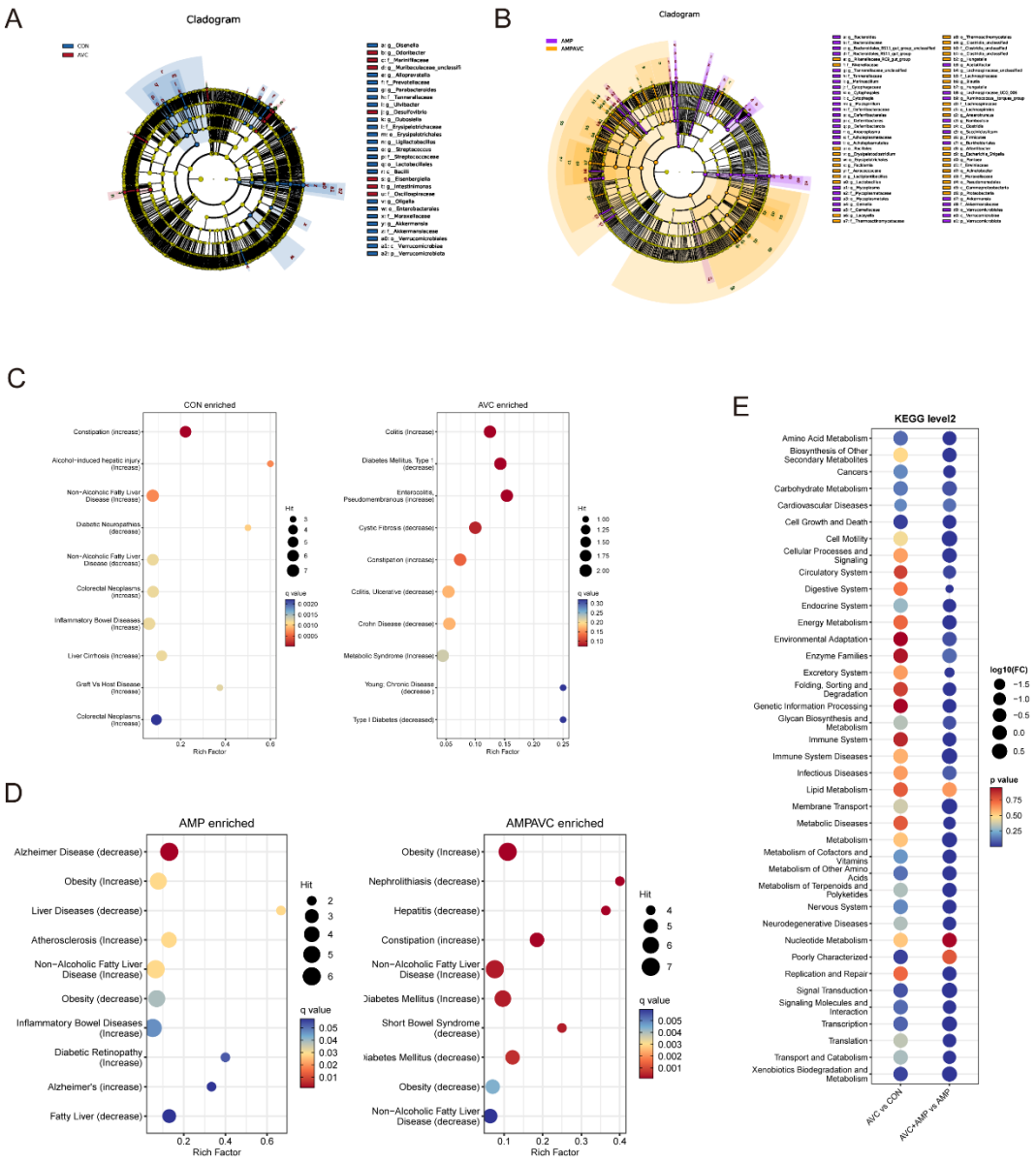

Figure S3. Bacteriome cannot explain MGP and blood glucose caused by antiviral cocktail. Related to Figure 2.

(A-B) LEfSe analysis identified the most differentially abundant taxons in (A) CON and (B) AMP background. LDA score > 3 and Wilcoxon< 0.05 are shown. Cladogram of significant changes at all taxonomic levels. The root of the cladogram represents the domain bacteria. The size of node represents the abundance of taxa. n = 5 mice/group.

(C-D) Bubble chart is used to display the TSEA result of MicrobiomeAnalyst's. The pool of bacteria was set by LEfSe result in (C) CON and (D) AMP background. The color of the bubbles represents the q-value, and the size of the bubbles represents Hit bacteria number.

(E) Bubble chart is used to display the stamp analysis of KEGG annotated pathways predicted by PICRUSt2 in cecal bacteriome treated by AVC and AMP. The color of the bubbles represents the p-value, and the size of the bubbles represents logFC. n = 5 mice/group.

Intestinal virome abundance was correlated with FCR and OGTT

While acknowledging the limitations of the gut bacteriome in elucidating the metabolic changes induced by AVC, we focused on the virome. We analyzed the cecal virome of CON and AVC groups, identifying 6,188 viral operational taxonomic units (vOTUs). Of these, 1,224 were known vOTUs listed in the IMG/VR database, and 4,964 were novel sequences (Figure 3A). Notably, the AVC group exhibited a higher count of vOTUs compared to the CON group (Figure 3A). However, diversity indices, such as Shannon and Simpson, were lower in the AVC group, indicating less diversity among dominant viral species (Figure 3A), aligning with recent findings of a reduced Shannon index in the gut viromes of obese and diabetes populations.[18] Further β-diversity analysis showed significant alterations in gut virome composition due to AVC treatment. (Figure 3B and 3C). Considering the pronounced reduction in gut virome quantity due to AVC, we normalized for the number of cecal VLPs and discerned that AVC treatment diminished

the abundance of *Microvitidae*, *Herelleviridae*, and *Rountreeviridae* families, while *Inoviridae*, *Circoviridae*, *Genomoviridae*, *Schitoviridae*, *Straboviridae*, and *Ackermannviridae* families increased. (Figure 3D).

With the substantial presence of novel vOTUs in our dataset, we directly assessed the correlation between these adjusted vOTUs and both FCR and OGTT. Intriguingly, correlation analysis uncovered a collection of vOTUs, predominantly from the Petitvirales order, associated with AVC-induced metabolic changes (Figure 3G). Given that bacteriophages can regulate bacterial metabolic functions through auxiliary metabolic genes[19], we compared the virome gene set with the KEGG database. KEGG function prediction analysis indicated that AVC treatment does not affect carbohydrate metabolism or glycan synthesis and metabolism pathways in virome (Figure S4A).

Reflecting on the intricate predator-prey interactions between bacteriophages and bacteria, it's crucial to acknowledge that even low-abundance organisms may significantly influence gut microbiome regulation[20]. We conducted a co-analysis of virome and bacterial data to pinpoint key viral or bacterial OTUs across both omics. Procrustes analysis indicated a weakened correlation between the bacteriome and virome post-AVC treatment (Firgure S4B). The unsupervised multiple co-inertia analysis (MCIA) mirrored single-omics PCoA results, with the first component clearly separating AVC and CON groups (Figure 3E). Utilizing Omicsanalyst2.0 for correlation network analysis[21], we identified 69 key OTUs, including 29 bacterial OTUs and 40 vOTUs. *Bacteroides*, *unclassified c1-61*, *Alloprevotella*, *Akkermansia*, and *Microviridae a4-12225* had the highest betweenness (betweenness≥150). Correlation analysis of these OTUs with FCR and OGTT revealed a series of vOTUs potentially associated with AVC-induced changes, most of which are unannotated (Figure 3H). Interestingly, VLPs abundance correlated positively with FCR and negatively with OGTT (Figure 3I). Compared to the bacteriome, the virome appears to have a stronger correlation with AVC-induced changes in FCR and OGTT.

These findings encourage us to pursue more rigorous methods to determine whether the gut virome can independently influence the small intestine, separate from the bacteriome.

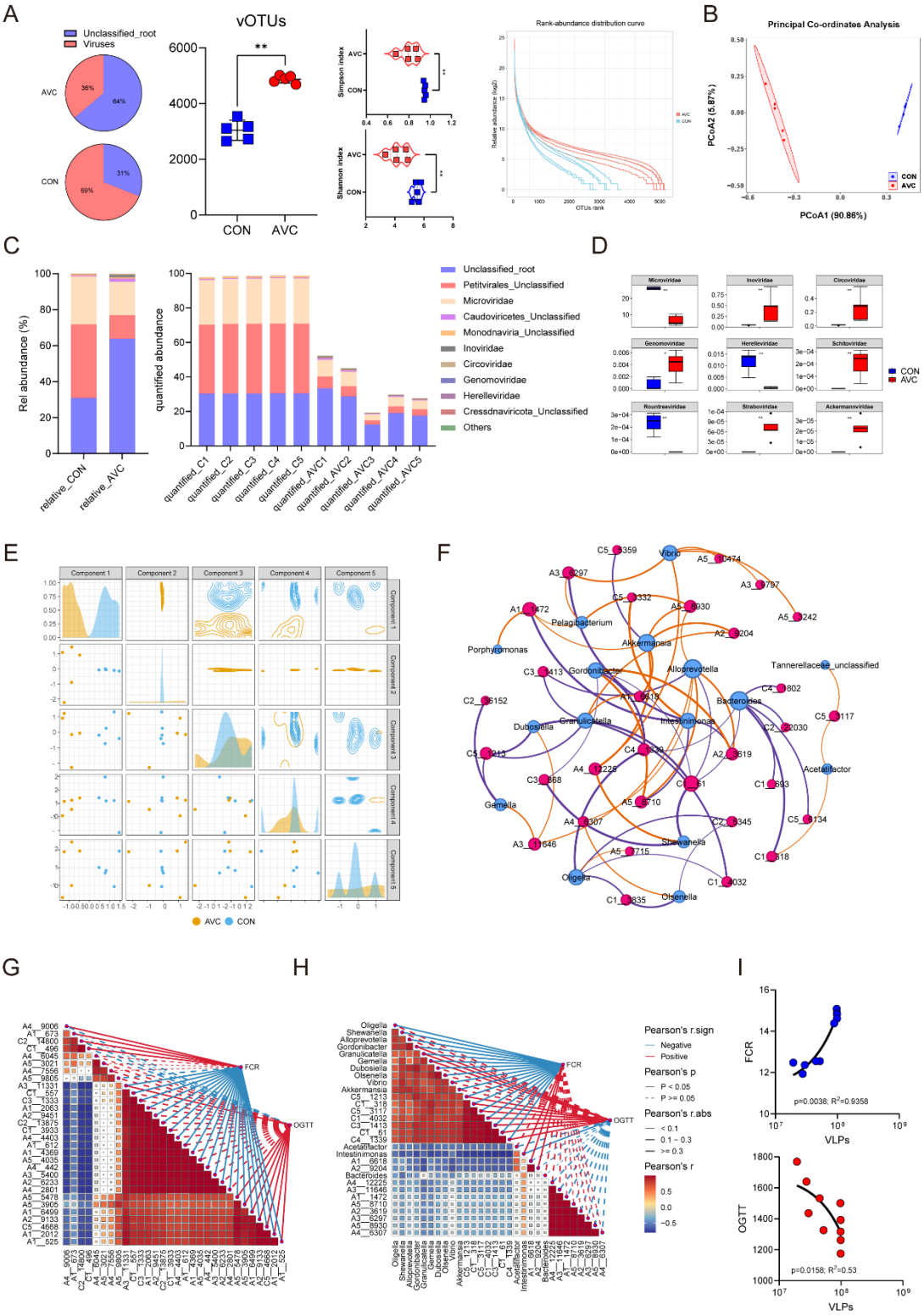

Figure 3. Intestinal virome abundance was positively correlated with FCR and negatively

correlated with OGTT.

(A) Novelty, Richness, Shannon's and Simpson's diversity for the cecal DNA virome. Kruskal-Wallis test, followed by Wilcoxon's rank sum test with Bonferroni's correction, was conducted for alpha diversity. n = 5 mice/group.

(B) Principal co-ordinates analysis (PCoA) of virome DNA sequencing of cecal content at the operational taxonomic unit level. n = 5 mice/group.

(C) Community barplot analysis of virome DNA sequencing of cecal content at the family level. n = 5 mice/group.

(D) Quantified abundance of viral family changed by AVC treatment. n = 5 mice/group.

(E) Pairwise component scores plot for the top five components of MCIA analysis.

(F) Correlation network of high-magnitude loadings from the top three components.The shown nodes are the feature OUT with absolute values greater than 0.75 between both bacterial and viral omics.

(G-H) The relationship between OTUs and FCR and OGTT in (I) virome DNA sequencing and (J) Multi-omics was calculated. The significant levels of Pearson's correlation among dependent variables were indicated by square size. Network planning showed the Pearson's correlation between top 30 OTUs and FCR and OGTT. Red lines indicate positive correlations, while blue lines indicate inverse correlations. Edge width corresponds to Pearson's r value, and edge type indicates statistical significance. Pearson's correlation coefficient matrix shows the relationships among dependent bacteria genus. The significant levels of Pearson's correlation among dependent bacteria genus were indicated by square size. Normality and Lognormality of FCR and OGTT were tested by Kolmogorov-Smirnov test, $p>0.1$.

(I) Simple linear regression illustrating the relationship between the number of VLPs in cecal content and FCR and OGTT.

(D) represents mean ± SD analyzed by Mann-Whitney test. $*p < 0.05$, $**p < 0.01$.

See also Figure S4.

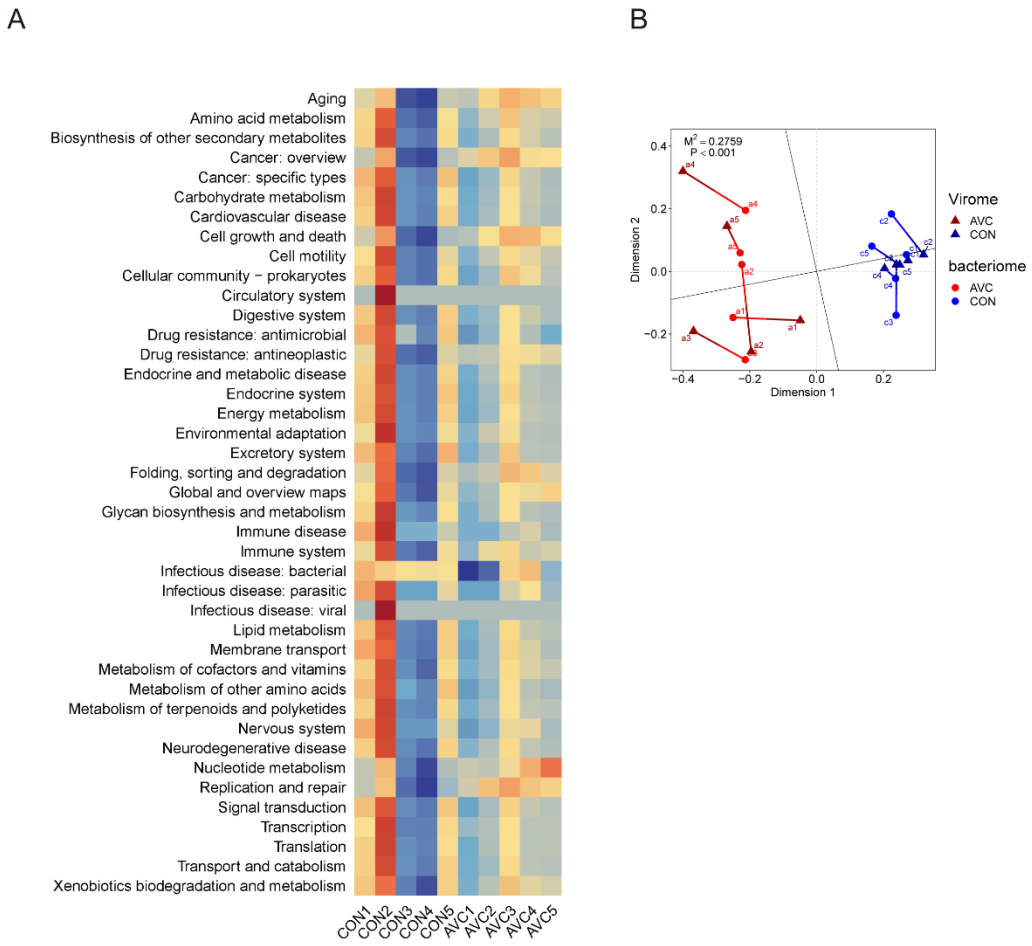

Figure S4. Intestinal virome abundance was positively correlated with FCR and negatively correlated with OGTT. Related to Figure 3.

(A) Heatmap is used to display the expression of KEGG annotated pathways predicted by METAProdigal in cecal virome.

(B) Procrustes analysis of the samples based on the bacteriome and virome. The shorter the line between bacteriome and virome, the more significant the correlation between them.

CVT alters the CD&A of the small intestine in GF and ABXT mice

To elucidate the distinct influence of the virome on small intestinal CD&A beyond the bacteriome, we employed germ-free (GF) mice, which offer a clean slate without bacterial interference. VLPs from cecal content of specific pathogen-free (SPF) mice were isolated,

317 ensuring no bacterial contamination (Figure S5A). These purified VLPs were then
318 administered to GF mice via oral gavage every three days over a four-week period
319 (Figure 4A). Following CVT (Cecal virome transplant), the mice exhibited a reduction in
320 body weight and an elevation in FCR, despite uniform food intake among the cohorts
321 (Figure 4B and S5B). Furthermore, the CVT group demonstrated a reduced area under
322 the OGTT curve (Figure 4B). Notably, these observations sharply contrasted with those
323 made in SPF mice receiving AVC (Figure 1C, 1I and 4B).
324
325 Single-cell RNA sequencing of the small intestine from GF CVT mice revealed a
326 decrease in enterocyte frequency and a concomitant increase in transit-amplifying (TA)
327 cells (Figure 4C, 4D and S6). CD&A gene expression was suppressed in the CVT group,
328 whereas genes linked to fat digestion and absorption showed diverse expression levels
329 (Figure 4E). Further analysis of enterocytes revealed a positive correlation between high
330 expression of CD&A genes, *slc25a4*, *Rdh*, *Slc13a1* and *Slc10a2* expression, with no
331 significant changes observed in genes related to fat digestion and absorption, except
332 *Fabp2* (Figure 4F). These alterations in cell composition and gene expression suggest
333 the gut virome's involvement in small intestinal CD&A and epithelial remodeling.
334
335 Acknowledging the marked contrasts between GF and SPF mice[22], antibiotic-treated
336 mice (ABXT mice) were employed to determine if a brief period of CVT could influence
337 CD&A genes expression in the small intestine (Figure 4G). Post-antibiotic treatment fecal
338 plating confirmed the effectiveness of the antibiotics, with a significant decrease in VLPs
339 abundance observed (Figure S5C and S5D). Similar to GF mice, CVT in ABXT mice
340 suppressed the expression of CD&A (Figure 4H and 4I). Notably, even though the full
341 turnover of the intestinal epithelium usually takes 4-5 days[23], a short-term CVT still
342 managed to inhibit the expression of CD&A genes. This indicates that the virome's
343 control over CD&A may not rely solely on epithelial turnover. Besides, *in vivo*, AVC
344 promoted the expression of CD&A genes, with the exception of *slc5a9* (Figure 4J). To
345 isolate the effect of AVC drug on CD&A genes expression of intestinal epithelial cells

346 (IECs), we incubated primary intestinal crypts (ICs) with the same concentration of AVC
347 drug in drinking water. Intriguingly, we found that AVC only inhibited *slc5a1* expression,
348 while animal experiments revealed that AVC actually promotes *slc5a1* expression (Figure
349 S5E).
350
351 Collectively, these findings demonstrate that the gut virome itself possesses the ability to
352 drive intestinal epithelial remodeling and CD&A independently of the bacteriome.

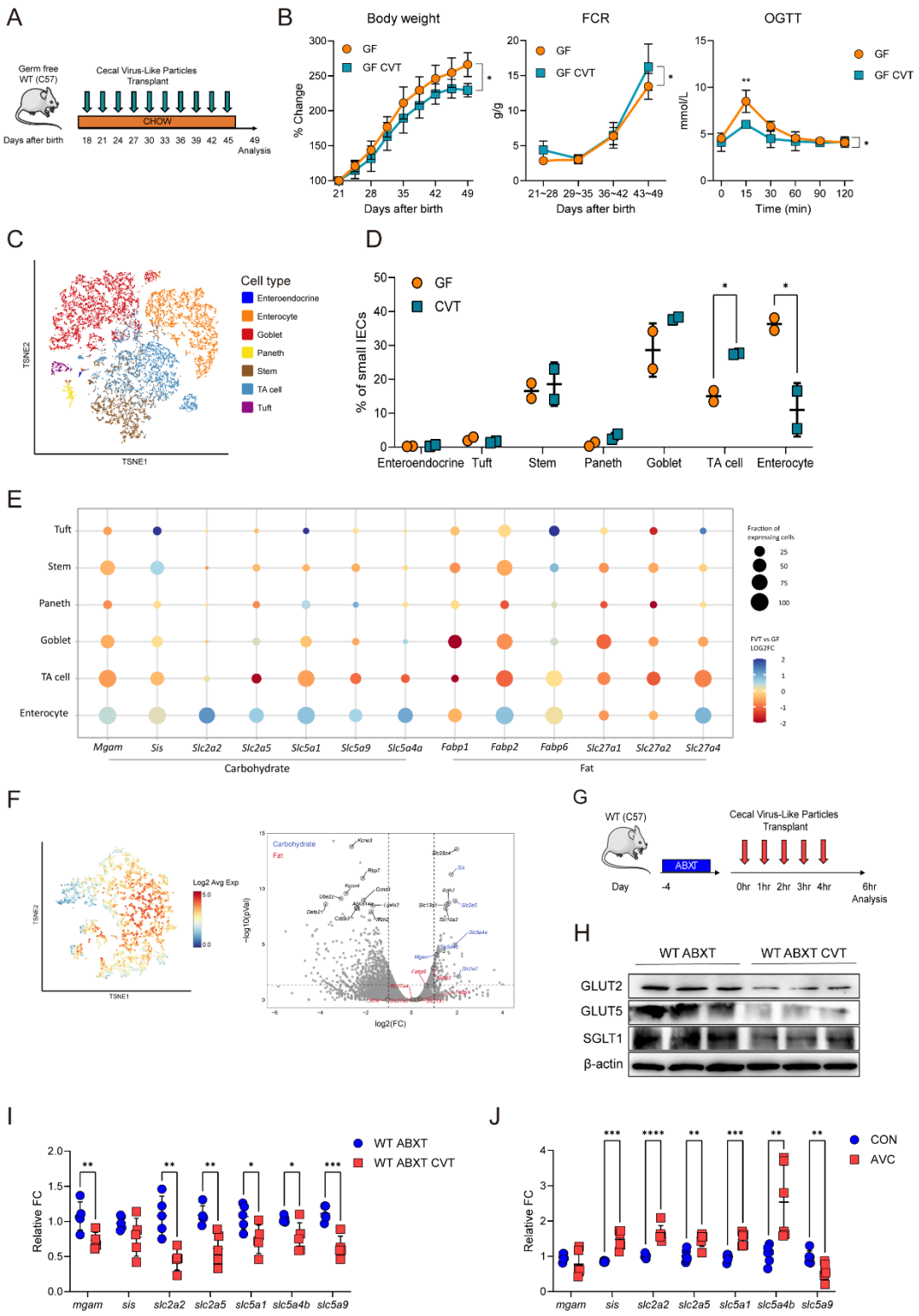

Figure 4. CVT alters the CD&A of the small intestine in GF and ABXT mice.

(A) Experimental scheme for (B).

(B) Body weight, FCR and OGTT test in GF mice on a chow diet.

(C) t-Distributed stochastic neighbor embedding (t-SNE) plots of major epithelial cell

358 subsets with 10,000 cells displayed.

359 (D) Frequency of epithelial cell subsets in (A) in GF CVT.

360 (E) Differential expression of macronutrient digestion and absorption for carbohydrates

361 and fat.

362 (F) Volcano plot showing differentially regulated genes in small intestinal epithelial cells

363 with high expression of CD&A genes. Colored circles correspond to transcripts for brush

364 border enzymes and transporters involved in digestion of carbohydrates and lipids.

365 (G) Experimental scheme for (H).

366 (H) and (I) represent western blot and qPCR analysis of CD&A genes expression in small

367 intestine in ABXT CVT mice. n = 5 mice/group.

368 (J) represents qPCR analysis of CD&A genes expression in small intestine in AVC mice.

369 n = 5 mice/group.

370 (B) represent mean ± SD analyzed by two-way ANOVA with Geisser-Greenhouse

371 correction. (D), (H) and (I) represents mean ± SD analyzed by Student's t-test. Data

372 combined from two independent experiments. $*p < 0.05$, $**p < 0.01$, $***p < 0.001$.

373 See also Figure S5 and S6

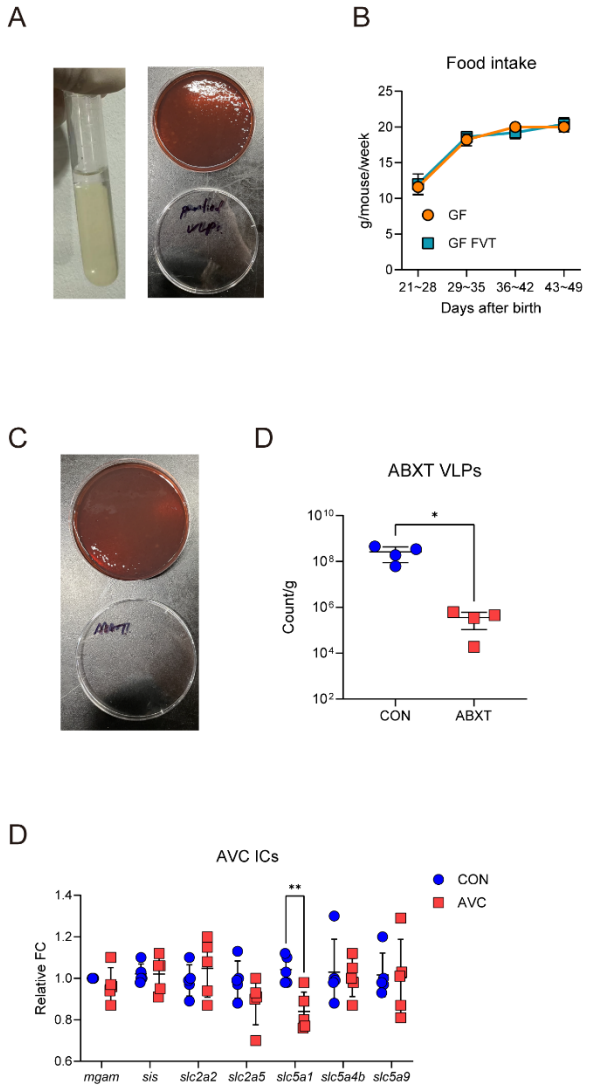

Figure S5. CVT alters the CD&A of the small intestine in GF and ABXT mice. Related to Figure 4

(A) Representative images of bacteria culture analysis on CBA plates and BHI Broth for purified VLPs.

(B) Food intake in GF mice on a chow diet. n = 6 mice/group.

(C) Representative images of bacteria culture analysis on CBA for ABXT mice cecum.

(D) The numbers of cecum VLPs stained with SYBR Gold for before and after ABXT treatment. n = 4 mice/group.

(E) qPCR analysis of CD&A genes expression in ICs stimulated with AVC drugs. n = 5

(B) represent mean ± SD analyzed by two-way ANOVA with Geisser-Greenhouse correction. (C) and (D) represents mean ± SD analyzed by Student's t-test. Data

386 combined from two independent experiments. *p < 0.05, **p < 0.01.

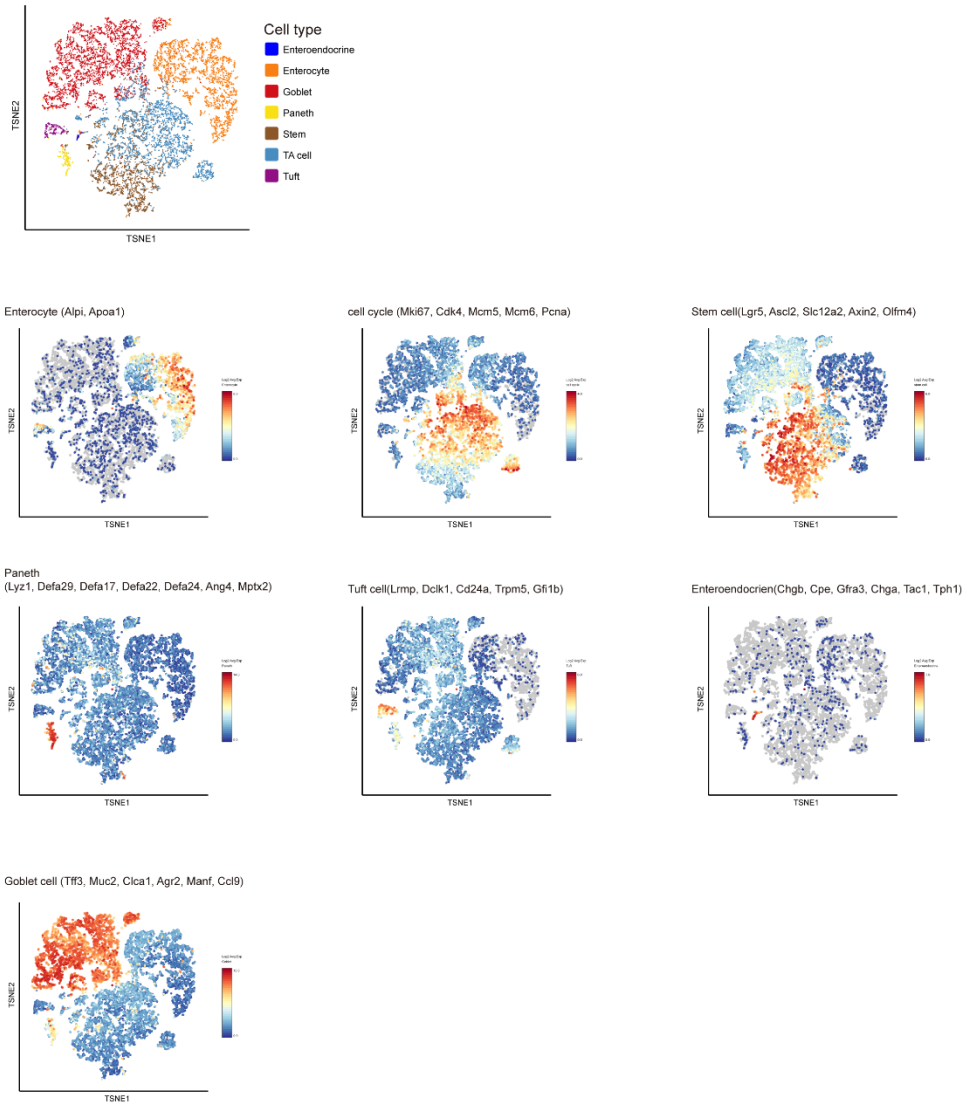

387

388 Figure S6. CVT alters the CD&A of the small intestine in GF and ABXT mice. Related to

389 Figure 4

390 Annotation of small intestinal epithelial cell types by scRNAseq. t-SNE visualization of

391 10,000 cells showing cell type annotation of known marker genes.

392 Viromes regulate small intestinal 393 CD&A via T cells

394 Considering the vital function of IECs in CD&A, our preliminary research examined if the

395 virome could suppress the CD&A in the small intestine through IECs interaction. VLPs

396 were incubated with ICs, followed by qPCR analysis of CD&A gene expression.
397 Surprisingly, contrary to our *in vivo* findings, VLPs promoted CD&A gene expression in
398 ICs in a dose-dependent manner (Figure 5A). To delve deeper into these *in vitro* findings,
399 we separated VLPs into their constituent parts: free DNA, capsids, and
400 Lipofectamine2000-encapsulated VLP DNA. The capsids showed no effect on CD&A
401 gene activity in ICs. Conversely, free DNA suppressed CD&A genes, whereas
402 Lipofectamine2000-encapsulated DNA activated Caco2 cells similarly to how VLPs
403 activated ICs (Figure. 5B, S7A and S7B).
404
405 Addressing the discrepancy between *in vivo* and *in vitro* outcomes, we explored the
406 virome's potential impact on other small intestine cells, particularly immune cells. T cells
407 and innate lymphoid cells (ILCs) are recognized for their significant role in modulating
408 nutrient detection in the small intestine[7,8]. We administered fluorescent-labeled VLPs to
409 ABXT mice and analyzed intestinal cells using flow cytometry an hour later. Fluorescence
410 microscopy and flow cytometry verified that overnight dialysis using 100 kDa membranes
411 successfully eliminated free SYBR Gold dye (Figure S7C and S7D). Notably,
412 CD11c+F4/80+ cells ingested VLPs (Figure. 5C). Additionally, immunofluorescence
413 analysis revealed an increase in T cell infiltration in the small intestine (Figure. 4D).
414
415 To assess whether VLPs activated antigen-presenting cells (APCs) have an increased
416 ability to attract T cells, proximity labeling experiments were conducted. The results
417 demonstrated that VLP-activated APCs had a heightened capacity to recruit T cells,
418 indicating the virome's influences both APCs and T cells (Figure S7D). Subsequently, we
419 found that CD&A genes of ICs were suppressed by APCs-T cells (Figure 5E).
420 Considering the involvement of APCs, we stimulated APCs-T cells with only capsids and
421 discovered that capsids alone had a stronger inhibitory effect on ICs CD&A than
422 complete VLPs (Figure 5F). Capsids transplant also exhibited results similar to CVT in
423 ABXT mice (Figure 5G).
424

425 Due to the potent inhibitory role of T cells in CD&A, we replicated the AVC experiments
426 using T cell-deficient BALB/NUDE mice. AVC treatment did not induce any alterations in
427 MGP or OGTT in BALB/NUDE mice (Figure. 5H). ABXT CVT experiments in BALB/NUDE
428 mice shown that CVT did not only suppress the expression of CD&A, but also promoted
429 the expression of *slc2a2*, *slc2a5*, and *slc5a1* (Figure 5I and 5J). Lymphocytes isolated
430 from the small intestines of BALB/NUDE mice, were unable to suppress CD&A genes
431 expression, even promoting the expression of *slc5a9* (Figure 5K). These findings suggest
432 that the inhibition of CD&A by VLPs is T-cell dependent, with APCs alone being
433 insufficient for such inhibition. RNA-sequencing of small intestinal tissue from both WT
434 and BALB/NUDE mice treated with ABXT CVT revealed that CVT suppressed CD&A
435 gene expression in WT mice but did not affect genes associated with amino acid or fat
436 digestion and absorption (Figure 5L, S7F and S7G). In BALB/NUDE mice, CVT was not
437 observed to impact the digestion and absorption of any macronutrients (Figure 5L, S7F
438 and S7G).
439
440 RNA sequencing has delineated a distinct pattern of gene expression in response to CVT.
441 Compared WT with BALB/NUDE mice, a significant portion of these genes were
442 depended T cell (Figure. S7H). K-means analysis revealed that CVT-related genes
443 expression changes is contingent upon T cell involvement (Figure. S7I). Most of these
444 genes are associated with the immune system and T cell function (Figure. S7J). These
445 findings collectively underscore the pivotal role of T cells in the virome's regulatory effects
446 on the small intestine.
447
448 Collectively, our findings illuminate the intricate interplay between the gut virome, immune
449 cells, and IECs nutrient sensing. The virome directly and indirectly influences CD&A gene
450 expression through its interaction with both IECs and immune cells, particularly T cells.

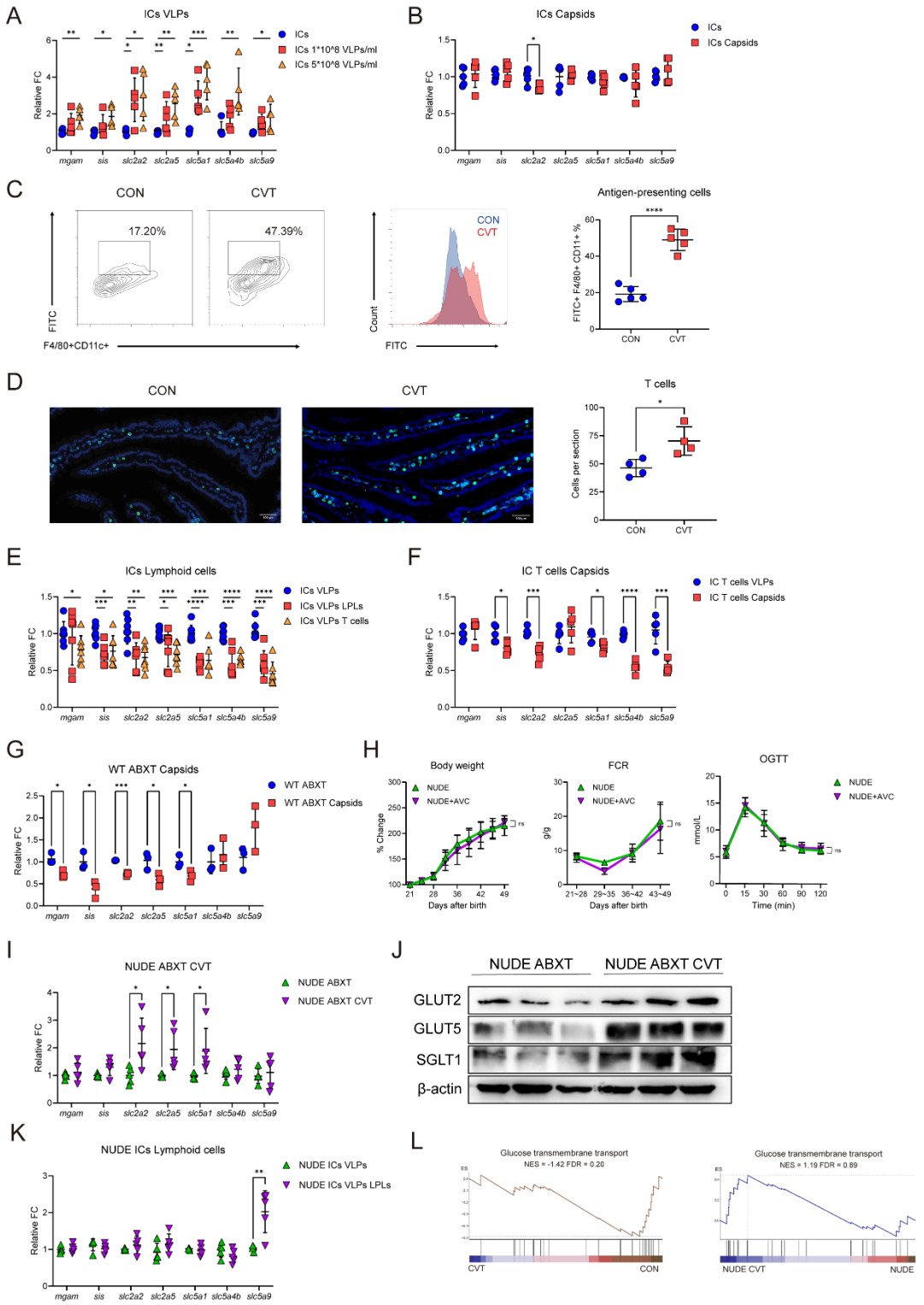

Figure 5. Viromes regulate small intestinal CD&A via T cells.

(A) and (B) represent qPCR analysis of CD&A genes expression in ICs stimulated with (A) VLPs or (B) protein capsids. n = 5

(C) Flow cytometry for APCs from the small intestine of SYBR Gold-stained VLPs

transplant mice. n = 5

(D) Immunofluorescence staining for CD45 (cyan) and CD3 (green) in the intestine of CVT-treated mice.

(E-G) represent qPCR analysis of CD&A genes expression in ICs stimulated with LPLs, T cells and protein capsids.

(H) Body weight and FCR in BALB/NUDE mice on a chow diet. n = 6 mice/group

(I) and (J) represent qPCR analysis and western blot of CD&A genes expression in small intestine of BALB/NUDE mice treated with CVT. n = 5 mice/group

(K) represent qPCR analysis of CD&A genes expression in ICs stimulated with leukocytes from small intestine of BALB/NUDE mice. n = 5 mice/group

(L) GSEA of genes upregulated or downregulated in glucose transmembrane transport in WT-CVT and BALB/BUDE CVT. Normalized enrichment scores (NES) and false discovery rates (FDR) are shown.

(A-G) and (I-J) represents mean ± SD analyzed by Student's t-test. (H) represent mean ± SD analyzed by two-way ANOVA with Geisser-Greenhouse correction. Data combined from two independent experiments. $*p < 0.05$, $**p < 0.01$, $***p < 0.001$.

See also Figure S7.

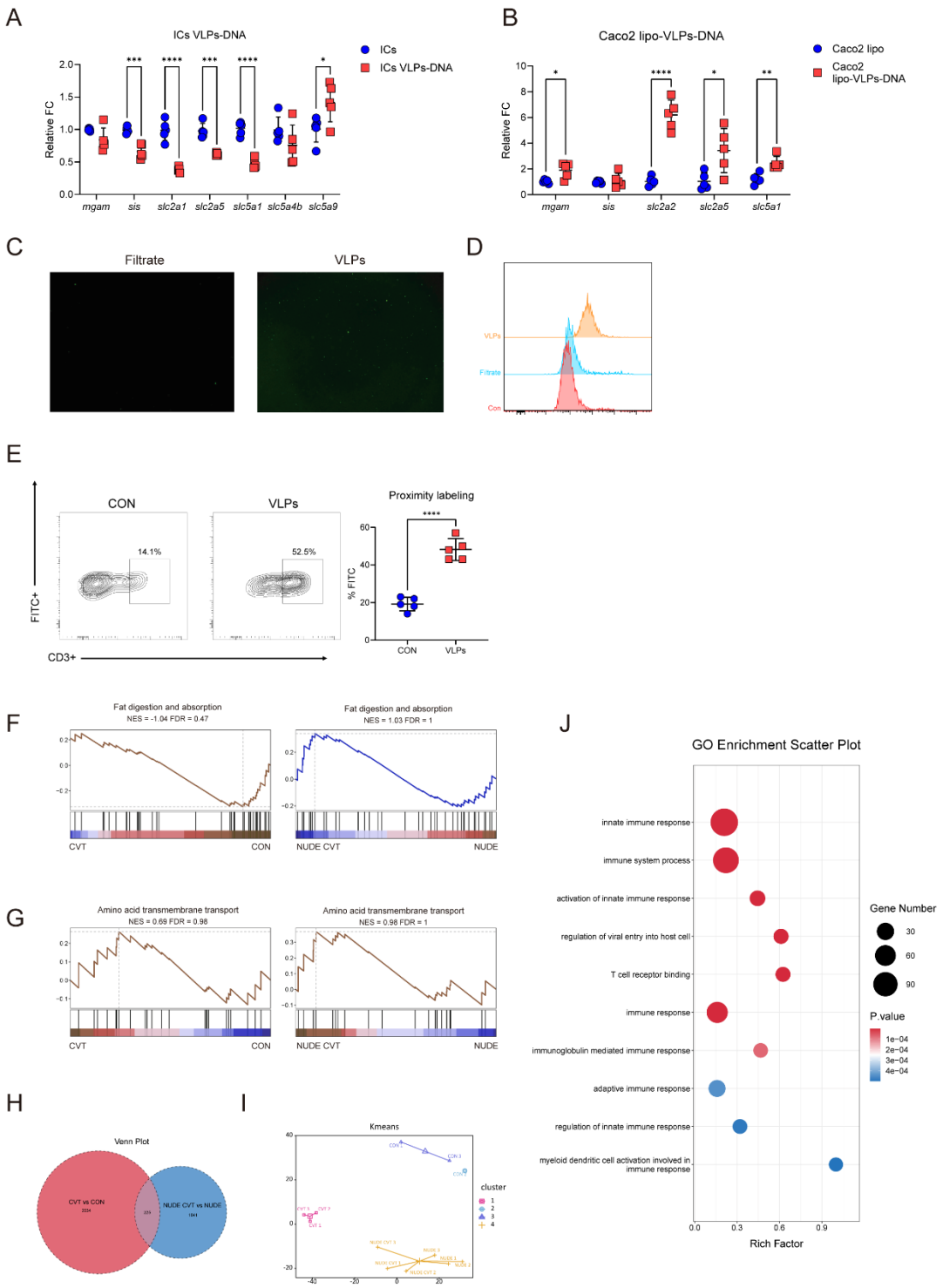

Figure S7. Viromes regulate small intestinal CD&A via T cells. Related to Figure 5. (A) and (B) represent qPCR analysis of CD&A genes expression in ICs and Caco2 stimulated with (A) VLPs DNA or (B) Lipofectamine2000-packaged VLPs DNA. n = 5 (C) and (D) Test the remained SYBR Gold dye by (C) Confocal imaging and (D) flow

cytometry.

(E) Flow cytometric analysis of antigen-specific fucosyl-biotinylation in T cells when incubated with APCs primed with VLPs. n = 5

(F) and (G) represent GSEA of genes upregulated or downregulated in (F) Fat digestion and absorption and (G) amino acid transmembrane transport in WT-CVT and BALB/BUDE CVT.

(H) Venn diagram depicting the changed genes of the small intestine of WT-CVT and BALB/NUDE CVT.

(I) K-means analysis of differentially expressed genes in both WT-CVT and BALB/NUDE mice.

(J) Bubble chart is used to display the changed genes in Gene Ontology (GO) analysis within the set of (CVT versus CON)\(NUDE_CVT versus NUDE_CON).

(A) and (B) represent mean ± SD analyzed by Student's t-test. $*p < 0.05$, $**p < 0.01$, $***p < 0.001$.

Virome inhibit the carbohydrate transcriptional program by Th17 cells-IL22

Recognizing the pivotal function of T cells, we investigated whether CVT alters cytokine receptor expression in the small intestine. A comparison between WT and BALB/NUDE mice revealed a pronounced influence of CVT on the interleukin 22 (IL22) receptor in WT mice (Figure 6A). IL22 is known to regulate the intestinal barrier and nutrient sensing[24]. GSEA showed increased activity in IL22 receptor-related pathways, such as stat protein phosphorylation and the Pi3k-Akt signaling pathway, in WT mice following CVT treatment, a response absents in BALB/NUDE mice (Figure 6B and 6C). *In vitro*, co-incubation of VLPs with ICs demonstrated that VLPs alone could stimulate *IL22ra1* expression in ICs (Figure 6D). When VLPs were co-incubated with APCs and T cells, there was an increase in IL22 expression in Th17 cells (Figure S6E and S6F). However, VLPs did not

induce IL22 in innate ILC3s, which are another primary IL22 producers in the small intestine [25](Figure S8A). It is known that the development of intestinal Th17 cells and the synthesis of IL22 are dependent on aryl hydrocarbon receptor (AHR), retinoic acid receptor-related orphan receptor (ROR), and IL23 receptor (IL23r)[26]. VLPs were found to stimulate the expression of *Rora* in Th17 cells and *Wnt5a* in APCs (Figure S8B and S8C). Further, treating ICs with IL22 showed that IL22 could suppress the expression of CD&A genes, an effect enhanced by VLPs. (Figure 6G and 6H).

To determine if T cells' suppressive effect on CD&A genes depended on IL22, we blocked IL22 with an antibody before co-incubation. The results indicated that the suppressive effect of T cells was largely nullified, except for *mgam* and *slc5a4b*, highlighting the gut virome's crucial role in regulating intestinal CD&A through IL22. (Figure 6I and 6J).

Previous studies suggest that IL22 can activate the MAPK and Pi3k-Akt signaling pathways via stat protein phosphorylation[27]. Our GSEA analysis revealed an upregulation of only the Pi3K-Akt signaling pathway (Figure 6B, 6C, S8D and S8E). Stimulation of ICs with IL22 did not alter Akt protein level, but increase the phosphorylation of Akt (Figure S8F). Chromium picolinate, a Pi3k-Akt signaling pathway agonist, could mimic the effects of IL22, promoting Akt phosphorylation and inhibiting CD&A genes expression (Figure S8G and S8H).

Research has shown that viral proteins can have sequences akin to eukaryotic cytokines and exhibit biological activity[28]. Utilizing the NCBI BLAST database, we scrutinized the gut virome—focusing on bacteriophages—to unearth sequences resembling cytokines that could play a role in Th17 cell maturation, IL22 secretion, and the modulation of CD&A gene expression in IECs. (Table S5). Our investigation revealed bacteriophage sequences with significant similarity to cytokine proteins (e value< 0.05), particularly within the PFAM domains of these targets (Table S5, S6 and S7). Notably, sequences from *Siphoviridae* bacteriophages paralleled amino acids 98-133 of IL17A, aligning with

its PFAM domain (amino acids 70-148)[29]. Similarly, Caudovirales phages matched amino acids 57-117 of IL6, corresponding to its PFAM domain (amino acids 37-222)[30]. Then, we predicted the structure of phage fragments and corresponding cytokine receptors by alphafold3.0[31]. Among these models, *Caudovirales* phage fragment similar to IL6 (phage-sIL6) and the IL6 receptor interaction showcased the highest compatibility scores (ipTM = 0.33, pTM = 0.57). IL6 is known to directly influence T cells, triggering STAT3 activation and fostering the expression of Th17-specific transcription factors RORγt and RORα, thus encouraging Th17 cell differentiation[32]. The phage-sIL6 structure predicted by AlphaFold3.0 mirrors the IL6 sequence, adopting a Helix-β-strand-Helix configuration (FigureS9A and S9B). Furthermore, the co-predicted interaction between phage-sIL6 and the IL6 receptor suggests potential biological activity, akin to the IL6-IL6 receptor binding, particularly at the Fibronectin type-III 1 and 2 domains (residues 182–186, residues 294–30) (Figure S9C and S9D).

These findings highlight the complex interplay between the gut virome, immune cells, and IECs nutrient sensing, and underscore the multifaceted role of the virome in regulating small intestinal physiology and metabolism.

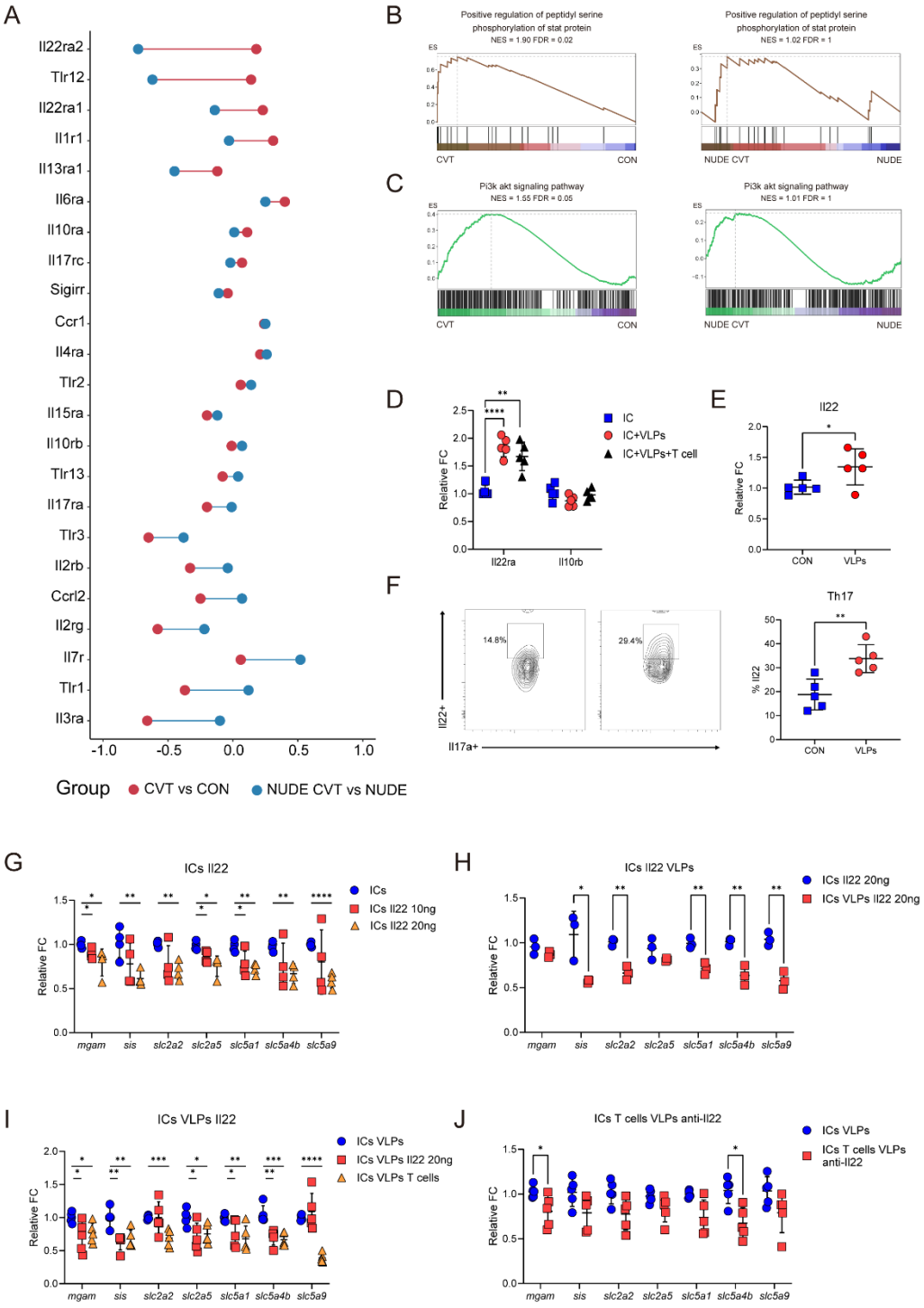

Figure 6. Virome inhibit the carbohydrate transcriptional program by Th17 cells-IL22.

(A) Dumbbell plot is used to display the changed cytokine receptor genes in WT-CVT and BALB/NUDE CVT.

(B) and (C) represent GSEA of genes upregulated or downregulated in IL22 signal

556 pathway related-(B) Positive regulation of peptidyl serine phosphorylation of stat protein
557 and (C) Pi3k Akt signaling pathway in WT-CVT and BALB/BUDE CVT.
558 (D) represents qPCR analysis of *Il22ra1* expression in ICs stimulated with VLPs and T
559 cells. n = 5
560 (E) and (F) represent (E) qPCR analysis and (F) flow cytometry of *Il22* and IL22
561 expression in Th17 cells stimulated with APCs and VLPs. n = 5
562 (G) and (H) represent qPCR analysis of CD&A genes expression in ICs stimulated with
563 (G) IL22 alone and with (H) IL22 and VLPs. n = 5
564 (I) and (J) represent qPCR analysis of CD&A genes expression in ICs stimulated with (G)
565 T cells and with (H) IL22 antibody blocking T cells. n = 5
566 (D-J) represents mean ± SD analyzed by Student's t-test. $*p < 0.05$, $**p < 0.01$, $***p <$
567 0.001.
568 See also Figure S8 and S9

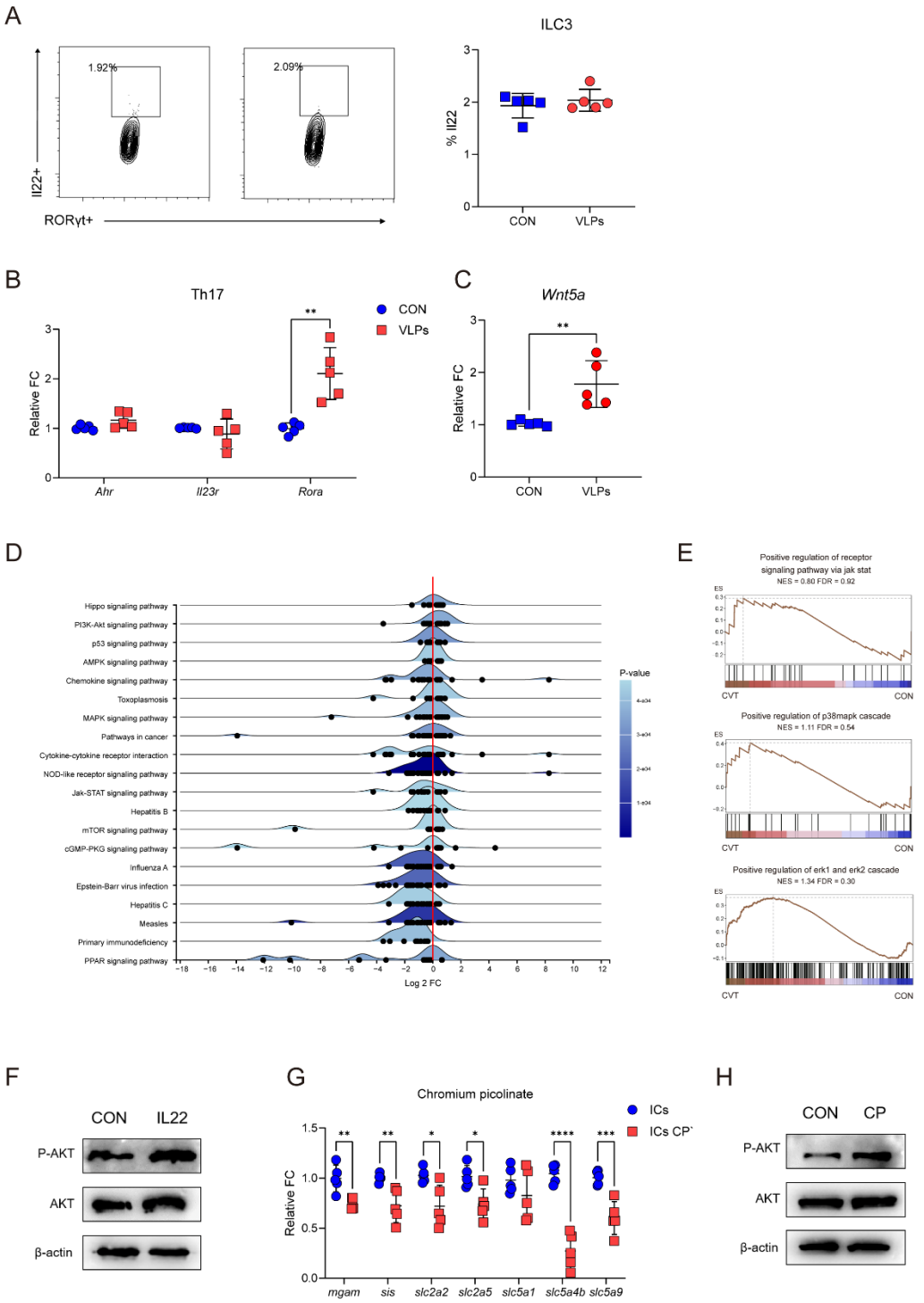

Figure S8. Virome inhibit the carbohydrate transcriptional program by Th17 cells-IL22. Related to Figure 6

(A) Flow cytometry for IL22 of IC3s stimulated with VLPs. n = 5

(B) and (C) represent qPCR analysis of the growth and development of intestinal Th17

cells and the synthesis of IL22 related genes expression in (B) Th17 cells and (C) APCs. n = 5

(D) Ridgeline plot is used to display the changed genes in KEGG analysis within the set of (CVT versus CON)∖(NUDE_CVT versus NUDE_CON).

(E) represents GSEA of genes upregulated or downregulated in IL22 signal pathway related-positive regulation of receptor signaling pathway via jak stat, positive regulation of p38mapk cascade and positive regulation of erk1 and erk2 cascade.

(F) represents Western blot of Akt and phosphorylated Akt in ICs stimulated with or without IL22.

(G-H) represents (G) qPCR analysis of CD&A genes expression and (H) Western blot of Akt and phosphorylated Akt in ICs and stimulated Chromium picolinate. n = 5

(A-C) and (G) represents mean ± SD analyzed by Student's t-test. $*p < 0.05$, $**p < 0.01$, $***p < 0.001$.

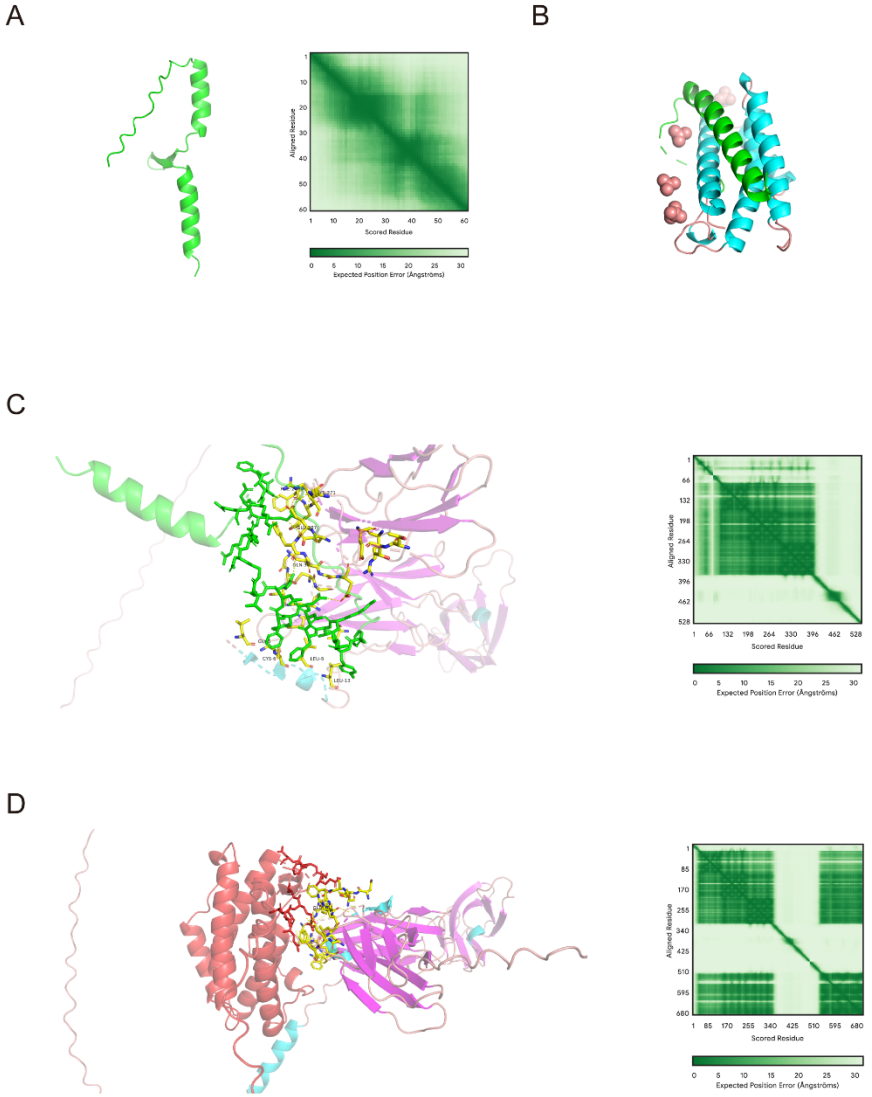

Figure S9. Virome inhibit the carbohydrate transcriptional program by Th17 cells-IL22. Related to Figure 6

(A), (C), and (D) represent the whole-length-predicted structural model of (A) phage-sIL6, (C) phage-sIL6 (Green) and IL6 receptor and (D) IL6 (Red) and IL6 receptor with prediction alignment error score heatmap. The yellow sticks represent the residues on the IL6 receptor within the 5Å range of phage-sIL6 or IL6. The axes indicate the position of the amino acids. Reliability of pairwise relative positions of amino acids is color coded from green (0 Å) to white (30 Å).

(B) represents the whole-length-predicted structural model of IL6 measured by W Somers et al. via X-ray.

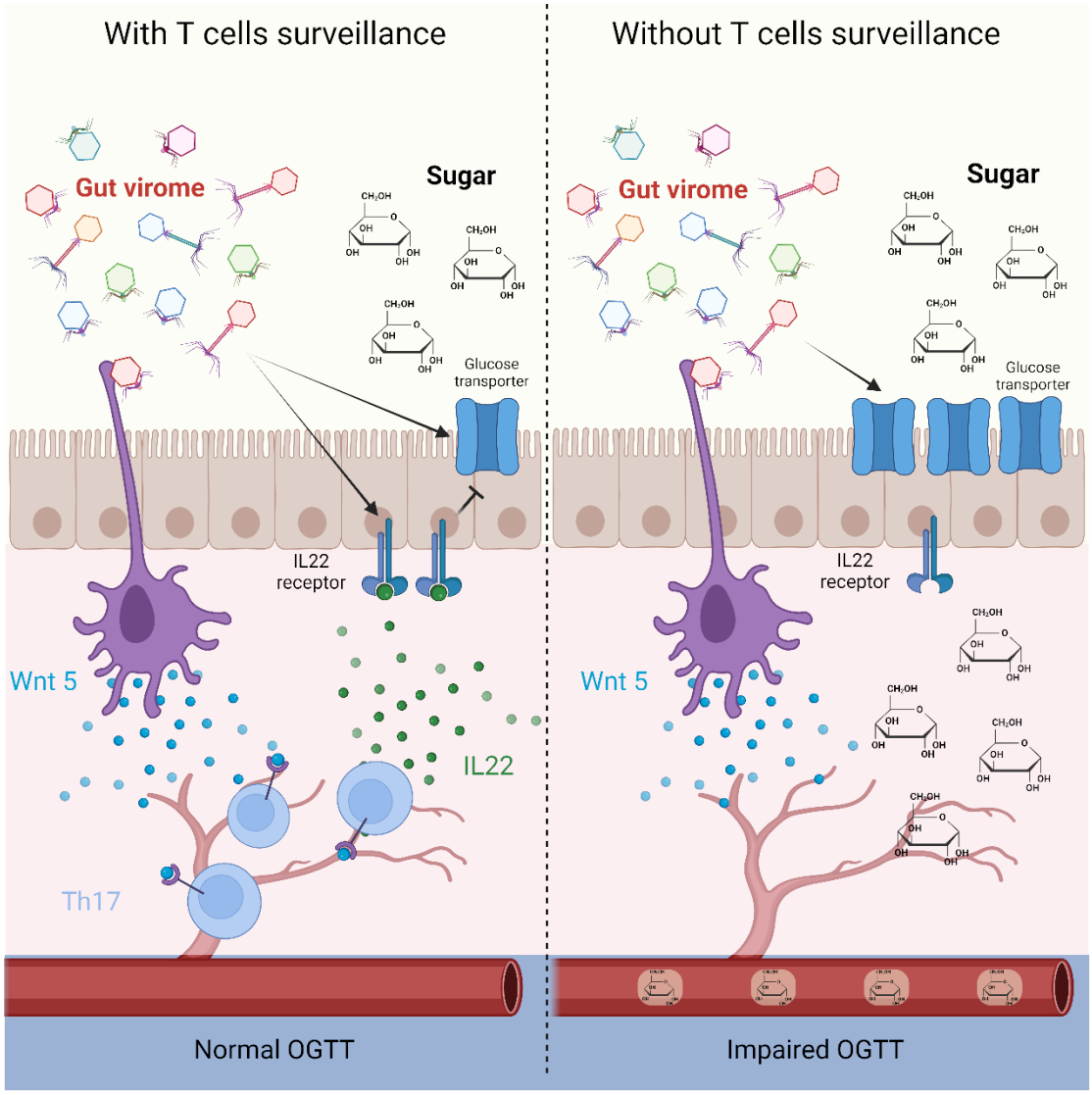

Figure S10. Interaction between the gut virome and small intestinal cells.

Under normal conditions, the gut virome directly stimulates the expression of CD&A genes and IL22 receptors in IECs, yet it is also recognized by APCs. APCs stimulated by the virome exhibit increased expression of *Wnt5*, enhancing the recruitment capability of T cells. Recruited T cells secrete IL22, which subsequently inhibits the expression of CD&A genes in IECs to maintain glucose homeostasis. However, in the absence of T cell surveillance, the gut virome stimulates the expression of CD&A genes in IECs, favoring glucose absorption into the bloodstream and leading to impaired glucose tolerance in murine hosts. Created with BioRender.com.

Discussion

The gut microbiota, nutritional substrates, and cellular components collectively facilitate the small intestine's nutrient management. Dysregulation of gut microbiota and inflammatory responses has been substantiated as a contributing factor in the etiology and progression of metabolic syndrome[33]. As evidenced by our findings, the gut virome directly influences eukaryotic cells and impacts the immune and metabolic landscape of the mouse small intestine. These insights are crucial for creating targeted treatments and dietary approaches for metabolic disorders.

Our research utilized a tripartite animal model—AVC, GF, and ABXT mice—to investigate the gut virome's role in macronutrient sensing in the small intestine. The AVC model, which diminishes the gut virome abundance, is conventionally utilized to inversely investigate the virome's systemic impact[34]. Challenging previous research, we found that AVC significantly alters the gut bacteriome's diversity. This underscores the need to include GF and ABXT mice in comprehensive virome studies.

We observed that the virome's regulation of CD&A is multifaceted. A recent study reported that the gut virome from healthy mice can alleviate HFD induced glucose impairment and obesity, and indicates that its protective effect is dependent on the bacteriome[3]. In our study, we also found that AVC does not affect the MGP and lipid accumulation in tissue of 60% HFD mice, but it can change those of mice on a chow diet and 45% HFD. In addition to lipids, dietary sugars are considered harmful to metabolic diseases, but their underlying mechanisms are unclear[35]. Our experiments show that gut virome can stimulate intestinal eukaryotic cells independent of bacteria to change the small intestine's CD&A. In the future, when formulating dietary plans, in addition to considering the gut bacteriome and lipids, the gut virome and carbohydrates should also be taken into account.

Next, we investigated the interactions between viral components and different types of

638 small intestinal cells. We have discovered that various viral components elicit distinct
639 responses in ICs, and only Lipofactime2000 packaged VLPs DNA replicating intact VLPs'
640 effects, suggesting a need for intracellular entry to function. Consistent with other
641 research, viruses mainly activate intracellular receptors, such as toll-like receptor 9 and
642 cyclic GMP-AMP synthase[36]. In addition to IECs, the small intestine harbors a vast
643 population of immune cells. Recent studies have pointed out that *in vitro*, dendritic cells
644 and macrophages will actively take up bacteriophage, but their significance is unclear[4,37].
645 We discovered that APCs will capture the gut virome and enhance their ability to recruit T
646 cells. Our study delves into the interactions between APCs and T cells, aiming to discern
647 if T cell-driven suppression of CD&A relies on capsids. We first determined that capsids
648 have no effect on the expression of CD&A genes in ICs. However, mirroring the CVT
649 model, capsid transplantation similarly curtails CD&A gene expression. These findings
650 suggest that viral capsids could be considered potential antigens, extending beyond the
651 nucleic acid.
652
653 IL22 is crucial for small intestinal health[25]. We discovered that Th17 cells suppress small
654 intestinal CD&A genes via IL22, a process enhanced by the virome. The virome not only
655 stimulates Th17 cells to express IL22, but also directly promotes the expression of IL22
656 receptor in ICs. IL22 receptor is expressed in various cell types and has pleiotropic
657 effects in metabolic diseases[38]. Whether the commensal virome has other regulatory
658 mechanisms for Th17 cells and epithelial cells needs further study.
659
660 Our work delineates the intricate interplay among diet, the gut virome, and intestinal cells.
661 Our findings further reveal that different gut virus components elicit heterogeneous
662 responses in various cell types. Future therapeutic and nutritional strategies for metabolic
663 diseases should incorporate the gut virome as a significant factor of intervention.
664

METHODS

Mice

All animal experiments conducted in this study were approved by the Experimental Animal EthICs Committee of Jinling Hospital affiliated to Medical School of Nanjing University. C57/BL6J and BALB/NUDE mice were sourced from Nanjing GemPharmatech Co. Sterile C57/BL6J mice were bred and housed in a sterile mouse facility at Nanjing GemPharmatech Co. Male mice aged 3 weeks were utilized for the AVC experiments, while those aged 6-8 weeks were used for other experiments. All feeds were irradiated and sterilized. Mice had *ad libitum* access to food and water, with the AVC and AMP drinking water changed every two days. The AVC formula consisted of ribavirin (0.2 mg/ml), acyclovir (0.25 mg/ml), and lamivudine (0.6 mg/ml), while AMP was administered at a concentration of 1 g/L. For ABXT, mice received sterilized water supplemented with AMP (0.1 mg/mL), neomycin trisulfate salt hydrate (10 mg/mL), metronidazole (10 mg/mL), and vancomycin hydrochloride (5 mg/mL), with a volume of 10 μL/g body weight[39]. Detailed dietary compositions are provided in Table S1.

Glucose tolerance test

After a 12-hour fast, mice underwent an OGTT, where glucose was administered orally at a dosage of 2g/kg. Blood samples were obtained from the tail vein at 0, 15, 30, 60, 90, and 120 minutes post-glucose challenge for glucose measurement using Accu-Chek glucose meters.

Enumeration of cecum VLPs

The cecum contents were resuspended in SM buffer at a ratio of 1:5 (SM buffer: 8 mM magnesium sulfate heptahydrate, 50 mM Tris-Cl, 100 mM NaCl, and 0.01% gelatin)[40]. After homogenization for 5 minutes, the mixture was centrifuged at 2700 g for 15 minutes. The supernatant was collected and centrifuged at 17000 g for 15 minutes, repeating until no precipitate was observed. Next, 0.2 volume of peg buffer (peg buffer: 200g/L peg8000, 2.5M

690 NaCl) was added, and the mixture was left in an ice bath overnight. The following day,
691 centrifugation was performed at 3300 g for 1 hour. The supernatant was discarded, and the
692 precipitate was resuspended in SM buffer. Then, 0.3 volume of chloroform was added, gently
693 mixed, and centrifuged at 2500g for 5 minutes and collect the aqueous phase.

694 Histological examination

695 The liver, E-WAT, and intestine tissue samples were fixed in 4% phosphate-buffered
696 formaldehyde, paraffin-embedded, and subsequently stained with hematoxylin and eosin.

697 Immunofluorescence

698 Slides were incubated overnight at 4°C in a humid chamber with antibodies against CD3 and
699 CD45 (1:200 dilution), followed by incubation with biotinylated secondary antibody (1:500
700 dilution) for one hour. Images were captured using Olympus FV3000 confocal microscope
701 and Olympus OlyVIA system.

702 Quantification of VLPs by flow 703 cytometer and epifluorescence 704 microscopy

705 Adapted from the method by Mária Džunková et al[41], phage T7 and phage MS2 were stained
706 with SYBR Gold at 4°C for 30 minutes as a positive control. Ultrapure water was filtered
707 through a 100 kDa ultrafiltration tube, and the filtrate was used as a negative control. The
708 FITC channel sensitivity of the flow cytometer was set to the highest, and the cell size was set
709 to the lowest. T7, MS2, and filtrate were detected at the slowest flow rate, and bacteriophage
710 gates were drawn. Cecum VLPs were extracted using the aforementioned method. The VLPs
711 were then stained with SYBR Gold for 30 minutes and dialyzed through a 100 kDa
712 ultrafiltration membrane overnight. The dialyzed VLPs were detected by epifluorescence
713 microscopy. Particles with sizes <0.5 μm were considered VLPs.

Intestinal crypts isolation and treatment

The mouse small intestines were longitudinally cut and cleaned with PBS. Subsequently, the small intestine was cut into 5mm pieces and placed in pre-cooled 10mM EDTA/PBS buffer at 4°C, incubated on ice for 30 minutes. After vigorous shaking for 5 minutes, the mixture was allowed to stand for 5 minutes, and the supernatant was discarded. The precipitate was resuspended in 10mM EDTA/PBS buffer and subjected to another 30-minute ice bath[42]. After shaking again for 5 minutes, 5% FBS was added, followed by a 5-minute incubation period. The supernatant was filtered through a 70μm cell sieve. The purity and density of ICs were observed under a microscope. If the content of ICs was low, the precipitation was resuspended with 10mM EDTA/PBS buffer and the steps were repeated until clean ICs were obtained. The crypts were then centrifuged at 100g for 2 minutes, resuspended in FBS, and used for subsequent experiments.

Isolation of intestinal lymphocyte, T cells and APCs

The mouse small intestines were longitudinally cut and cleaned with PBS. Subsequently, the intestine was cut into 5 mm pieces and placed in pre-cooled 5 mM EDTA/PBS buffer at 4°C for 30 minutes on ice. After vigorous shaking for 5 minutes, the suspension was centrifuged at 300 g for 5 minutes, and the supernatant was discarded. The precipitate was then resuspended in collagenase III (100 U/ml) and incubated in a water bath at 37°C for 10 minutes. To stop the action of collagenase III, 5% FBS was added. The resulting cell suspension was filtered through a 40 μm cell sieve and centrifuged at 300 g for 5 minutes. After resuspending the pellet in 35% Percoll, it was layered slowly onto 75% Percoll for density centrifugation. Centrifugation at 700 g for 30 minutes resulted in the collection of the milky white cell layer[43], from which T cells and APCs were further extracted using a isolation kit as per experimental requirements.

Coculture of APCs, T cells and ICs

After co-incubating APCs with VLPs overnight, the cells were washed twice with PBS. An equal number of T cells were then added and co-incubated. Subsequently, $5*10^5$ T cells-APCs and ICs, derived from whole intestine extracts of one mouse, were co-incubated for 2 hours at 37°C and 5% CO_2 in a total volume of 1ml FBS.

Proximity labeling

APCs cells (1 million) were suspended in 100 μl HBSS and incubated on ice for 20 minutes with 0.2 mg/mL GDP-Fuc-FT. Following this, the cells were washed twice with DPBS and exposed to cecum VLPs at 37°C for 2 hours. Subsequently, the cells were rinsed twice with PBS. The intestinal APCs were then co-cultured with an equivalent number of T cells at 37°C for 2 hours. Afterward, GDP-Fuc-biotin was added to a final concentration of 50 μM, and the reaction was halted with LacNAc after 30 minutes[44]. FITC-streptomycin was utilized to stain the cells prior to flow cytometry analysis.

qPCR analysis

Tissue or cell was processed with the Trizol reagent according to the manufacturer's instructions to extract total RNA. Subsequently, the RNA was reverse transcribed to cDNA using a real-time kit from Invitrogen. Relative quantification of gene expression was performed using the comparative CT method, with *rpl13* or *GAPDH* serving as the internal controls. Primer sequences are provided in Table S8.

Extraction of VLPs protein capsids

After obtaining VLPs as described above, an 0.2 volume of 0.5 M EDTA was added and incubated at 65°C for 1 h. Cool on ice and then add DNase 1mg/ml at 37°C for 1 h, and heat inactivated DNase at 95°C for 15 minutes[40].

Extraction of VLPs DNA

After obtaining VLPs as described above, an equal volume of 0.5 M EDTA was added. DNA extraction was then performed using Phenol/Chloroform/Isoamyl alcohol (25:24:1) according to the manufacturer's instructions. Following precipitation with ammonium acetate at -20°C overnight, the supernatant was removed by centrifugation at 16,000g for 30 minutes. The resulting pellet was resuspended in 70% ethanol, centrifuged at 16,000g for 3 minutes, and the supernatant was discarded. The pellet was then dried at 65°C for 3 minutes, and the DNA was resuspended in TE buffer.

Viral DNA sequencing

The previously described method was employed to enrich cecum VLPs, followed by purification of E.Z.N.A.® Viral DNA Kit, in accordance with the manufacturer's instructions. Subsequently, library construction was conducted using the total DNA and TruSeq Nano DNA sample preparation Kit from Illumina, as per the manufacturer's protocol. Libraries were then size selected for DNA target fragments of ~400bp on 2% Low Range Ultra Agarose followed by PCR amplified using Phusion DNA polymerase for 15 PCR cycles. Next, all samples were sequenced by the Illumina NovaSeq 6000 platform. The raw paired end reads were trimmed and quality controlled by Trimmomatic. Host sequences were removed using the BWA tool, and the Megahit tool was utilized to assemble the remaining sequences. For the assembled genome, sequences > 2000bp were selected, and those sequences were performed virus identification using deepVirFinder (VirFinder score > 0.7, p value < 0.05), VirSorter2 (default), VIBRANT (default), IMG/VR (identify >= 90% & cove rage >= 75%), geNomad (default) and phabox (default) database. vOTUs were clustered using Mummer software to compare candidate virus sequences (similarity > 95%, coverage > 85%, the longest representative one). The novelty and completeness were check by blastn (max target seqs > 5, e value < 1e-5, outfmt < 6, num threads > 8) and checkv (default)[45-47].

Virome gene prediction and annotation

The open reading frames (ORFs) of vOUTs were predicted using METAProdigal. The gene set was searched against the KEGG databases to identify the proteins to retrieve their function annotations.

Bacterial DNA extraction and sequencing

Cecal contents underwent DNA extraction using the CTAB method as per the manufacturer's instructions[48]. The extracted total DNA was eluted in the elution buffer and subjected to PCR analysis. Subsequently, the samples were sequenced on an Illumina NovaSeq platform according to the manufacturer's instructions. Paired-end reads were sorted based on their unique barcode and then trimmed by removing the barcode and primer sequence. FLASH was utilized to merge the paired-end reads. Quality filtering of the raw reads was performed under specific conditions to obtain high-quality clean tags using fqtrim. Chimeric sequences were eliminated using Vsearch software. After dereplication using DADA2, a ASV feature table and feature sequence were obtained. Feature sequences were annotated with SILVA database.

Droplet-based scRNA-seq and analysis

Single-cell suspensions were performed according to the methods described by Zuri A. Sullivan et al[8]. Briefly, following the procurement of ICs as per the aforementioned protocol, ICs were dissociated with TrypLE Express for 1 minute at 37°C. The resultant single-cell suspension was subsequently filtered through a 40-μm mesh and stained for fluorescence-activated cell sorting (FACS) prior to single-cell RNA sequencing (scRNA-seq). Single-cell suspensions were loaded to 10x Chromium to capture 5000 single cell according to the manufacturer's instructions of 10X Genomics Chromium Single-Cell 3' kit (V3). The following

813 cDNA amplification and library construction steps were performed according to the standard
814 protocol. Libraries were sequenced on an Illumina NovaSeq 6000 sequencing system (paired-
815 end multiplexing run,150bp) at a minimum depth of 20,000 reads per cell.

816 RNA sequencing and analysis

817 Total RNA extraction was performed using Trizol reagent following the manufacturer's
818 protocol. Transcriptome libraries were constructed using the TruSeqTM RNA Sample
819 Preparation Kit from Illumina and sequenced on the Illumina NovaSeqTM 6000 platform,
820 generating 2 x 150 bp paired-end reads. Clean reads were aligned to the reference genome
821 by Hisat2 and Genome[49]. Differential expression genes were identified by calculating the
822 expression level of each transcript using the fragments per kilobase of exon per million
823 mapped reads method.

824 Western blot analysis

825 Frozen ICs were homogenized in RIPA lysis buffer supplemented. After centrifugation of the
826 lysates, protein concentration was estimated in the supernatant using a BCA Protein Assay
827 Kit. Total proteins (30 μg) were separated on 10% SDS-polyacrylamide gel and then
828 transferred to Immobilon®-P PVDF membrane. Membranes were blocked with 5% milk in
829 TBS 1× Tween 0.1% for one hour before being probed overnight at 4°C with primary
830 antibodies. After washing, membranes were incubated with secondary antibodies. Signals
831 were recorded by the Tanon 5200.

832 Bioinformatics

833 The Fasta format sequences of the proteins were was retrieved from the UniProt database
834 (Table S9). The bioinformatics search was performed by tBLASTn with a threshold e-value
835 ≤0.05 using the proteins we searched before as query sequences against bacteriophage
836 proteomes (NCBI taxonomic ID: 2100421, 2731619,156614). The sequences of protein were
837 modeled using AlphaFold3 for three-dimensional structure predictions[50]. PyMOL was used to

generate images of protein and peptides' structures.

Statistics

Statistical analyses, excluding sequencing analysis, were done using GraphPad Prism 10, with details provided in figure legends.

Data and code availability

16S rRNA and Metagenomics sequencing data have been deposited at Sequence Read Archive (SRA) of NCBI. Please contact the corresponding author to request the Accession numbers.

Transcriptomic sequencing data can be found in Gene Expression Omnibus (GEO) of NCBI. Please contact the corresponding author to request the Accession numbers.

This paper does not report original code.

All supplementary data needed for the reanalysis of the findings presented in this paper can be obtained from the lead contact upon request.

Reference

1 Nishijima, S. *et al.* Extensive gut virome variation and its associations with host and environmental factors in a population-level cohort. *Nat Commun* **13**, 5252 (2022). https://doi.org:10.1038/s41467-022-32832-w

2 Ritz, N. L. *et al.* The gut virome is associated with stress-induced changes in behaviour and immune responses in mice. *Nat Microbiol* **9**, 359-376 (2024). https://doi.org:10.1038/s41564-023-01564-y

3 Rasmussen, T. S. *et al.* Faecal virome transplantation decreases symptoms of type 2 diabetes and obesity in a murine model. *Gut* **69**, 2122-2130 (2020). https://doi.org:10.1136/gutjnl-2019-320005

4 Bichet, M. C. *et al.* Mammalian cells internalize bacteriophages and use them as a resource to enhance cellular growth and survival. *PLoS Biol* **21**, e3002341 (2023). https://doi.org:10.1371/journal.pbio.3002341

5 Mahony, J., Casey, E. & van Sinderen, D. The Impact and Applications of Phages in the Food Industry and Agriculture. *Viruses* **12** (2020). https://doi.org:10.3390/v12020210

6 Harada, L. K. *et al.* Biotechnological applications of bacteriophages: State of the art. *Microbiol Res* **212-213**, 38-58 (2018). https://doi.org:10.1016/j.micres.2018.04.007

7 Kawano, Y. *et al.* Microbiota imbalance induced by dietary sugar disrupts immune-mediated protection from metabolic syndrome. *Cell* **185**, 3501-3519.e3520 (2022). https://doi.org:10.1016/j.cell.2022.08.005

8 Sullivan, Z. A. *et al.* γδ T cells regulate the intestinal response to nutrient sensing. *Science* **371** (2021). https://doi.org:10.1126/science.aba8310

9 Han, J. *et al.* High-Fat Diet-Induced Weight Gain, Behavioral Deficits, and Dopamine Changes in Young C57BL/6J Mice. *Front Nutr* **7**, 591161 (2020). https://doi.org:10.3389/fnut.2020.591161

10 Kolodziejczyk, A. A., Zheng, D. & Elinav, E. Diet-microbiota interactions and personalized nutrition. *Nat Rev Microbiol* **17**, 742-753 (2019). https://doi.org:10.1038/s41579-019-0256-8

11 Janssens, Y. *et al.* Disbiome database: linking the microbiome to disease. *BMC Microbiol* **18**, 50 (2018). https://doi.org:10.1186/s12866-018-1197-5

12 Niu, H. *et al.* Akkermansia muciniphila: a potential candidate for ameliorating metabolic diseases. *Frontiers in Immunology* **15** (2024). https://doi.org:10.3389/fimmu.2024.1370658

13 Lu, Y. *et al.* MicrobiomeAnalyst 2.0: comprehensive statistical, functional and integrative analysis of microbiome data. *Nucleic Acids Res* **51**, W310-w318 (2023). https://doi.org:10.1093/nar/gkad407

14 Téllez, A. *et al.* Epidemiology, Clinical Features, and Outcome of Infective Endocarditis due to Abiotrophia Species and Granulicatella Species: Report of 76 Cases, 2000–2015. *Clinical Infectious Diseases* **66**, 104-111 (2017). https://doi.org:10.1093/cid/cix752

15 Bowman, J. P. in *The Prokaryotes: A Handbook on the Biology of Bacteria Volume 6: Proteobacteria: Gamma Subclass* (eds Martin Dworkin *et al.*) 920-930 (Springer New York, 2006).

16 Seegers, J. F. M. L., Bui, T. P. N. & de Vos, W. M. in *Probiotic Bacteria and Postbiotic Metabolites: Role in Animal and Human Health* (eds Naheed Mojgani & Maryam Dadar) 139-151 (Springer Singapore, 2021).

17 Amiri, P. *et al.* Role of Butyrate, a Gut Microbiota Derived Metabolite, in Cardiovascular Diseases: A comprehensive narrative review. *Frontiers in Pharmacology* **12** (2022). https://doi.org:10.3389/fphar.2021.837509

18 Yang, K. *et al.* Alterations in the Gut Virome in Obesity and Type 2 Diabetes Mellitus. *Gastroenterology* **161**, 1257-1269 e1213 (2021). https://doi.org:10.1053/j.gastro.2021.06.056

19 Howard-Varona, C. *et al.* Phage-specific metabolic reprogramming of virocells. *Isme j* **14**, 881-895 (2020). https://doi.org:10.1038/s41396-019-0580-z

20 Yu, X. *et al.* Gut phageome: challenges in research and impact on human microbiota. *Front Microbiol* **15**, 1379382 (2024). https://doi.org:10.3389/fmicb.2024.1379382

21 Zhou, G., Pang, Z., Lu, Y., Ewald, J. & Xia, J. OmicsNet 2.0: a web-based platform for multi-omics integration and network visual analytics. *Nucleic Acids Res* **50**, W527-w533 (2022). https://doi.org:10.1093/nar/gkac376

22 Kennedy, E. A., King, K. Y. & Baldridge, M. T. Mouse Microbiota Models: Comparing Germ-Free Mice and Antibiotics Treatment as Tools for Modifying Gut Bacteria. *Frontiers in Physiology* **9** (2018). https://doi.org:10.3389/fphys.2018.01534

23 Sprangers, J., Zaalberg, I. C. & Maurice, M. M. Organoid-based modeling of intestinal development, regeneration, and repair. *Cell Death Differ* **28**, 95-107 (2021). https://doi.org:10.1038/s41418-020-00665-z

24 Gaudino, S. J. *et al.* Intestinal IL-22RA1 signaling regulates intrinsic and systemic lipid and glucose metabolism to alleviate obesity-associated disorders. *Nat Commun* **15**, 1597 (2024). https://doi.org:10.1038/s41467-024-45568-6

25 Keir, M. E., Yi, T., Lu, T. T. & Ghilardi, N. The role of IL-22 in intestinal health and disease. *Journal of Experimental Medicine* **217** (2020). https://doi.org:10.1084/jem.20192195

26 Zúñiga, L. A., Jain, R., Haines, C. & Cua, D. J. Th17 cell development: from the cradle to the grave. *Immunological Reviews* **252**, 78-88 (2013). https://doi.org:https://doi.org/10.1111/imr.12036

27 Lindahl, H. & Olsson, T. Interleukin-22 Influences the Th1/Th17 Axis. *Front Immunol* **12**, 618110 (2021). https://doi.org:10.3389/fimmu.2021.618110

28 Altindis, E. *et al.* Viral insulin-like peptides activate human insulin and IGF-1 receptor signaling: A paradigm shift for host-microbe interactions. *Proc Natl Acad Sci U S A* **115**, 2461-2466 (2018). https://doi.org:10.1073/pnas.1721117115

29 Liu, S. *et al.* Crystal structures of interleukin 17A and its complex with IL-17 receptor A. *Nature Communications* **4**, 1888 (2013). https://doi.org:10.1038/ncomms2880

30 Somers, W., Stahl, M. & Seehra, J. S. 1.9 Å crystal structure of interleukin 6: implications for a novel mode of receptor dimerization and signaling. *The EMBO Journal* **16**, 989-997-997 (1997). https://doi.org:https://doi.org/10.1093/emboj/16.5.989

31 Abramson, J. *et al.* Accurate structure prediction of biomolecular interactions with AlphaFold 3. *Nature* (2024). https://doi.org:10.1038/s41586-024-07487-w

32 Kaminskiy, Y. & Melenhorst, J. J. STAT3 Role in T-Cell Memory Formation. *International Journal of Molecular Sciences* **23**, 2878 (2022).

33 Luck, H. *et al.* Regulation of obesity-related insulin resistance with gut anti-inflammatory agents. *Cell Metab* **21**, 527-542 (2015). https://doi.org:10.1016/j.cmet.2015.03.001

34 Yang, J. Y. *et al.* Enteric Viruses Ameliorate Gut Inflammation via Toll-like Receptor 3 and Toll-like Receptor 7-Mediated Interferon-β Production. *Immunity* **44**, 889-900 (2016). https://doi.org:10.1016/j.immuni.2016.03.009

35 Diniz, M. S., Tocantins, C., Grilo, L. F. & Pereira, S. P. The Bitter Side of Sugar Consumption: A Mitochondrial Perspective on Diabetes Development. *Diabetology* **3**, 583-595 (2022).

36 Kong, L. Z. *et al.* Understanding nucleic acid sensing and its therapeutic applications. *Exp Mol Med* **55**, 2320-2331 (2023). https://doi.org:10.1038/s12276-023-01118-6

37 Sweere, J. M. *et al.* Bacteriophage trigger antiviral immunity and prevent clearance of bacterial infection. *Science* **363** (2019). https://doi.org:10.1126/science.aat9691

38 Sasaki, T. *et al.* Innate Lymphoid Cells in the Induction of Obesity. *Cell Rep* **28**, 202-217.e207 (2019). https://doi.org:10.1016/j.celrep.2019.06.016

39 Tirelle, P. *et al.* Comparison of different modes of antibiotic delivery on gut microbiota depletion efficiency and body composition in mouse. *BMC Microbiol* **20**, 340 (2020). https://doi.org:10.1186/s12866-020-02018-9

40 Adiliaghdam, F. *et al.* Human enteric viruses autonomously shape inflammatory bowel disease phenotype through divergent innate immunomodulation. *Sci Immunol* **7**,

eabn6660 (2022). https://doi.org:10.1126/sciimmunol.abn6660

41 Džunková, M., Moya, A., Chen, X., Kelly, C. & D'Auria, G. Detection of mixed-strain infections by FACS and ultra-low input genome sequencing. *Gut Microbes* **11**, 305-309 (2020). https://doi.org:10.1080/19490976.2018.1526578

42 Chen, Y., Li, C., Tsai, Y.-H. & Tseng, S.-H. in *Organoids: Stem Cells, Structure, and Function* (ed Kursad Turksen) 215-228 (Springer New York, 2019).

43 James, O. J., Vandereyken, M. & Swamy, M. in *Innate Lymphoid Cells : Methods and Protocols* (ed Shoba Amarnath) 141-152 (Springer US, 2020).

44 Liu, Z. *et al.* Detecting Tumor Antigen-Specific T Cells via Interaction-Dependent Fucosyl-Biotinylation. *Cell* **183**, 1117-1133.e1119 (2020). https://doi.org:10.1016/j.cell.2020.09.048

45 Du, Y., Fuhrman, J. A. & Sun, F. ViralCC retrieves complete viral genomes and virus-host pairs from metagenomic Hi-C data. *Nature Communications* **14**, 502 (2023). https://doi.org:10.1038/s41467-023-35945-y

46 Yang, K. *et al.* Rhizosphere phage communities drive soil suppressiveness to bacterial wilt disease. *Microbiome* **11**, 16 (2023). https://doi.org:10.1186/s40168-023-01463-8

47 Niu, L. *et al.* Diversity and potential functional characteristics of phage communities colonizing microplastic biofilms. *Environmental Research* **219**, 115103 (2023). https://doi.org:https://doi.org/10.1016/j.envres.2022.115103

48 Allen, G. C., Flores-Vergara, M. A., Krasynanski, S., Kumar, S. & Thompson, W. F. A modified protocol for rapid DNA isolation from plant tissues using cetyltrimethylammonium bromide. *Nature Protocols* **1**, 2320-2325 (2006). https://doi.org:10.1038/nprot.2006.384

49 Kim, D., Paggi, J. M., Park, C., Bennett, C. & Salzberg, S. L. Graph-based genome alignment and genotyping with HISAT2 and HISAT-genotype. *Nat Biotechnol* **37**, 907-915 (2019). https://doi.org:10.1038/s41587-019-0201-4

50 Abramson, J. *et al.* Accurate structure prediction of biomolecular interactions with AlphaFold 3. *Nature* (2024). https://doi.org:10.1038/s41586-024-07487-w